RESEARCH ARTICLE

Analysis of Donor Pancreata Defines the Transcriptomic Signature and Microenvironment of Early Neoplastic Lesions

Eileen S. Carpenter[1,2], Ahmed M. Elhossiny[3], Padma Kadiyala[4], Jay Li[5], Jake McGue[6], Brian D. Griffith[6], Yaqing Zhang[6], Jacob Edwards[6], Sarah Nelson[6], Fatima Lima[6], Katelyn L. Donahue[7], Wenting Du[6], Allison C. Bischoff[7], Danyah Alomari[1], Hannah R. Watkoske[6], Michael Mattea[8], Stephanie The[9], Carlos E. Espinoza[6], Meredith Barrett[6], Christopher J. Sonnenday[6], Nicholas Olden[10], Chin-Tung Chen[11], Nicole Peterson[12], Valerie Gunchick[12], Vaibhav Sahai[2,12], Arvind Rao[2,3,9,13,14], Filip Bednar[2,6], Jiaqi Shi[2,15], Timothy L. Frankel[2,6], and Marina Pasca di Magliano[2,6,16]

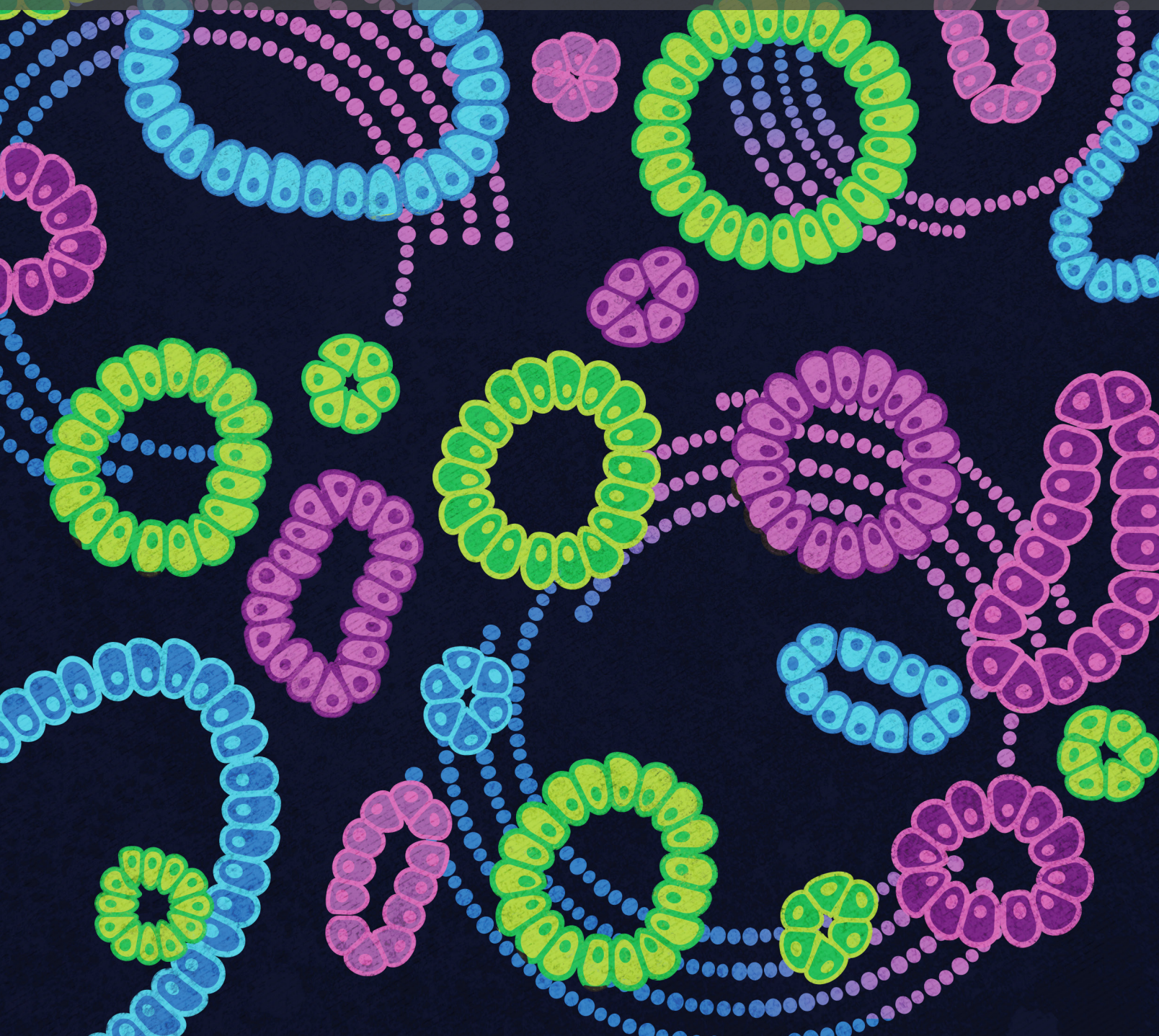

ABSTRACT The adult healthy human pancreas has been poorly studied given the lack of indication to obtain tissue from the pancreas in the absence of disease and rapid postmortem degradation. We obtained pancreata from brain dead donors, thus avoiding any warm ischemia time. The 30 donors were diverse in age and race and had no known pancreas disease. Histopathologic analysis of the samples revealed pancreatic intraepithelial neoplasia (PanIN) lesions in most individuals irrespective of age. Using a combination of multiplex IHC, single-cell RNA sequencing, and spatial transcriptomics, we provide the first-ever characterization of the unique microenvironment of the adult human pancreas and of sporadic PanIN lesions. We compared healthy pancreata to pancreatic cancer and peritumoral tissue and observed distinct transcriptomic signatures in fibroblasts and, to a lesser extent, macrophages. PanIN epithelial cells from healthy pancreata were remarkably transcriptionally similar to cancer cells, suggesting that neoplastic pathways are initiated early in tumorigenesis.

SIGNIFICANCE: Precursor lesions to pancreatic cancer are poorly characterized. We analyzed donor pancreata and discovered that precursor lesions are detected at a much higher rate than the incidence of pancreatic cancer, setting the stage for efforts to elucidate the microenvironmental and cell-intrinsic factors that restrain or, conversely, promote malignant progression.

See related commentary by Hoffman and Dougan, p. 1288.

INTRODUCTION

The pancreas, a main source of digestive enzymes, is uniquely susceptible to degradation postmortem (1–4). As there is no indication to sample the human pancreas in the absence of a pathology, our understanding of this organ is limited and has so far not benefited from advances in technology such as the single-cell revolution of the last decade. Pancreatic ductal adenocarcinoma (PDAC), the most common and deadly form of pancreatic cancer, arises from the exocrine pancreas (5, 6). Different precursor lesions precede overt malignancy, including mucinous lesions, which can be seen on imaging and surgically treated as indicated (7–10). In contrast, pancreatic intraepithelial neoplasia (PanIN) is microscopic and typically only encountered following resection of other pancreatic pathologies, including overt cancer (11–13). Autopsy studies—mostly in an older patient population—indicate that PanIN is common in older individuals; however, poor preservation of the pancreas due to prolonged warm ischemic time severely limits molecular analysis of autopsy samples (14–18). The prevalence of PanIN in the general healthy population remains unknown.

Pancreatic cancer is characterized by the accumulation of an extensive fibroinflammatory microenvironment, rich in the extracellular matrix and including cellular components such as fibroblasts and immune cells. Genomic studies have characterized the mutation profiles of primary and metastatic tumors and reinforced the notion that the *KRAS* gene is almost invariably mutated in pancreatic cancer, together with the common loss of tumor suppressor genes (19–22). Over the past several years, the advent of single-cell technologies has given us unprecedented insight into the cellular composition of the tumor microenvironment, the heterogeneity across and within populations, and the signaling pathways driving cellular cross-talk (23–26). Pancreatic cancer is also characterized by the accumulation of immune cells, including myeloid and lymphoid components; myeloid cells are largely immunosuppressive, whereas T cells are exhausted in the majority of patients with cancer (27–30). Whether corresponding populations of fibroblasts, myeloid cells, and T cells are present in the healthy human pancreas is unknown. A key limitation is that control samples are largely constituted by the adjacent normal pancreas; while lacking malignant tumor cells, these samples are often not histologically normal and present with extensive inflammation and other alterations. PanIN studies, while revealing that these

[1]Department of Internal Medicine, Division of Gastroenterology and Hepatology, University of Michigan, Ann Arbor, Michigan. [2]Rogel Cancer Center, University of Michigan, Ann Arbor, Michigan. [3]Department of Computational Medicine and Bioinformatics, University of Michigan, Ann Arbor, Michigan. [4]Immunology Graduate Program, University of Michigan, Ann Arbor, Michigan. [5]Medical Scientist Training Program, University of Michigan, Ann Arbor, Michigan. [6]Department of Surgery, University of Michigan, Ann Arbor, Michigan. [7]Cancer Biology Program, University of Michigan, Ann Arbor, Michigan. [8]Department of Molecular and Integrative Physiology, University of Michigan, Ann Arbor, Michigan. [9]Cancer Data Science Resource, University of Michigan, Ann Arbor, Michigan. [10]Gift of Life Michigan, Ann Arbor, Michigan. [11]Colorectal Cancer Research Center, Memorial Sloan Kettering Cancer Center, New York, New York. [12]Department of Internal Medicine, Division of Hematology and Oncology, University of Michigan, Ann Arbor, Michigan. [13]Department of Radiation Oncology, University of Michigan, Ann Arbor, Michigan. [14]Department of Biostatistics, University of Michigan, Ann Arbor, Michigan. [15]Department of Pathology, University of Michigan, Ann Arbor, Michigan. [16]Department of Cell and Developmental Biology, University of Michigan, Ann Arbor, Michigan.

Note: E.S. Carpenter, A.M. Elhossiny, and P. Kadiyala contributed equally to this article.

Corresponding Authors: Marina Pasca di Magliano, Rogel Cancer Center, Room 6306, 1500 East Medical Center Drive, Ann Arbor, MI 48109. Phone: 734-936-9083; E-mail: marinapa@med.umich.edu; and Timothy L. Frankel, Rogel Cancer Center, Room 6322, 1500 East Medical Center Drive, Ann Arbor, MI 48109. Phone: 734-615-1269; E-mail: timofran@med.umich.edu

Cancer Discov 2023;13:1324–45

doi: 10.1158/2159-8290.CD-23-0013

lesions share a similar mutation profile as cancer samples (refs. 10, 31–35; bioRxiv 2023.01.27.525553), are largely conducted in tissue from patients with cancer or patients with different pancreatic pathologies, based on paraffin-stored samples. Thus, our understanding of the microenvironment of the human pancreas and of early lesions is extremely limited. Although mouse models have been instrumental to understanding the early stages of pancreas carcinogenesis and to studying the healthy organ (36–39), they are a poor substitute for human samples. Mice are short-lived; laboratory mice spend their lives in a highly controlled environment with a specified diet, activity levels, and light/dark cycle and none of the environmental and lifestyle stressors that characterize human life.

Here, we describe a unique partnership between the Pancreatic Disease Initiative at the University of Michigan and Gift of Life Michigan, a centralized organ procurement and allocation center located less than 6 miles from the University Hospital and its laboratories. Although efforts are made to offer every organ to potential recipients in need, confounding factors often exist, including underlying disease of the donor (i.e., diabetes and obesity) or, commonly, exhaustion of the recipient list, which preclude transplantation, rendering organs available for research. This is particularly true for organs procured in donation after brain death (DBD). Unlike traditional organ donation in which death occurs following cardiovascular decline and subsequent hypotension and hypoxia, DBD maintains blood flow to organs until they can be rapidly flushed with a physiologic solution and immediately cooled to just above freezing. We posit these organs to be ideal for research analysis in which limitation of hypoxia, electrolyte imbalance, and rapid cooling will maximally preserve the cellular and transcriptomic profile of the normal pancreas. Our partnership with Gift of Life Michigan and close physical proximity has allowed for the analysis of pancreata from 30 DBD donors of varied age, race, and sex, resulting in a first-ever comprehensive map of the microenvironment of the organ in humans. Additionally, because donors are brought to the Gift of Life Donor Care Center from across the state of Michigan, there is a broad range of ethnicity, socioeconomic status, and environmental exposure, magnifying the applicability of these findings.

RESULTS

The Adult Human Pancreas Harbors Frequent PanIN Lesions

Through a collaboration with the Gift of Life Michigan organ and tissue program, we collected 30 pancreata from healthy adult organ donors for whom no suitable recipient was identified. Of note, all donors were prescreened via cross-sectional imaging and lab values (amylase and lipase) prior to organ recovery and were found to have no identifiable pathology in the pancreas. The organs were dissected from surrounding tissue, and superior mesenteric and celiac arteries were isolated. The arteries were cross-clamped and a cooled, isotonic physiologic solution was infused for 15 minutes. The organ was then rapidly removed and placed in a sterile solution at 4°C and transported to the University of Michigan for processing within 90 minutes of cross-clamp time (Fig. 1A). This method allows for no warm ischemic time, preserving the transcriptomic profile of the pancreas. As a pilot, we compared cell viability in samples from DBD with donation after circulatory death (DCD). In the latter, the heart and lungs are allowed to stop typically after a period of hypoxia and hypotension. This method is associated with a warm ischemic time of approximately 30 to 90 minutes, resulting in a dramatic decrease in pancreatic cell viability of less than 20%; we thus discontinued the DCD program (Supplementary Fig. S1A). Patient age spanned from the third to eighth decade of life and included 20 males and 10 females. Our patient cohort included about two of three white donors, one of three Black donors, one Asian donor, and one donor of unknown race, closely reflecting the demographic makeup of the state of Michigan (Fig. 1B; clinical table in Supplementary Table S1). For each sample, we collected 15 tissue blocks from multiple regions along the head–tail axis (Supplementary Fig. S1B). Histopathologic analysis of each block revealed PanINs in 18 of 30 donor specimens (Fig. 1B and C; refer to data availability statement for access to full slide scans) as well as normal acinar parenchyma, normal ducts, and areas of acinar-to-ductal metaplasia (ADM; Supplementary Fig. S1C). PanIN distribution ranged from isolated lesions in one region of the pancreas to multifocal. PanINs were surrounded by an area of fibrosis with interspersed cellular components (Fig. 1C).

PanINs from Healthy Individuals Are Surrounded by a Unique Microenvironment

To characterize the immune and stromal composition of the PanIN microenvironment, we performed multiplex fluorescent IHC (mfIHC) on formalin-fixed, paraffin-embedded (FFPE) tissue. We used a previously described immune panel (ref. 24; Fig. 2A; Supplementary Fig. S2A) and a newly optimized fibroblast panel (Fig. 2B; Supplementary Fig. S2B). We then quantified cellular composition in areas including PanIN compared with areas including normal acini, ducts, or ADM. Myeloid cells were enriched in ADM and PanIN areas compared with areas surrounding normal acini and ducts; CD4 T cells [but not regulatory T cells (Treg)] were notably detected around PanINs and ADM when compared with acinar cells and normal ducts (Fig. 2A and C). Abundant fibroblasts surrounded both normal ducts and PanINs, although the latter showed more heterogeneous staining for vimentin, αSMA, PDGFRb, and fibroblast activation protein (FAP; Fig. 2B and D), possibly indicating higher complexity of subtypes. Thus, PanIN formation is accompanied by the establishment of a unique microenvironment rich in fibroblasts, myeloid cells, and T cells, distinct from the histologically normal pancreas.

To gather further insight into the composition of PanIN and its microenvironment, we performed single-cell RNA sequencing of six donor organs for a total of 44,068 cells (Fig. 3A). For

Figure 1. The adult human pancreas harbors frequent PanIN lesions. **A,** Schematic of workflow to recover and process Gift of Life donor pancreas organs. **B,** Right, population distribution bar plot of the donor cohort. Tan bars represent donors that were found to have PanIN lesions on histologic examination. Blue bars represent donors in whom no neoplastic lesions were found. Left, pie chart of donor cohort by sex. Middle, pie chart of donor cohort by race. **C,** Hematoxylin and eosin (H&E) sections of representative PanIN lesions found in donor pancreata. Each H&E section represents a different donor.

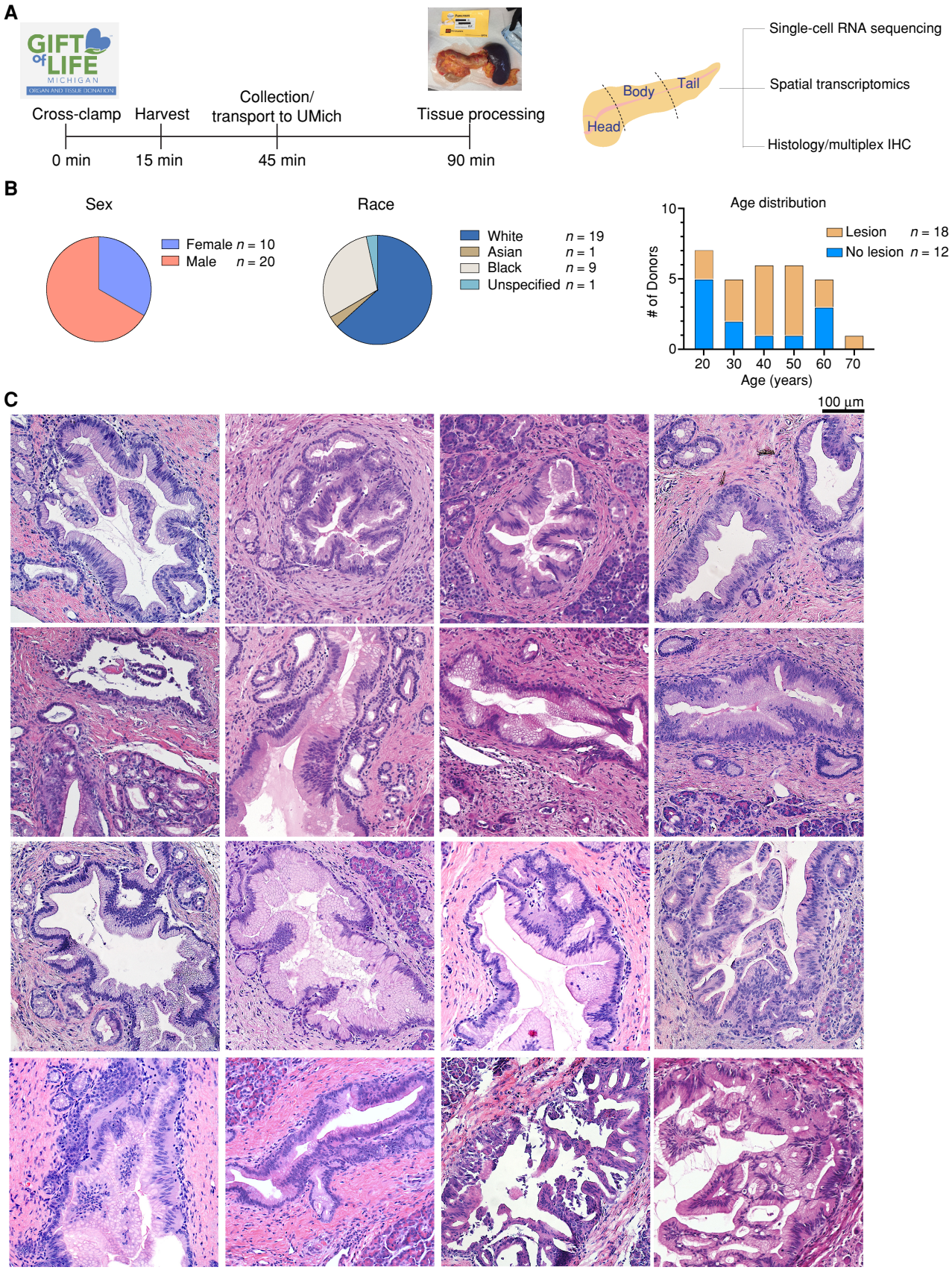
A
GIFT of LIFE MICHIGAN
ORGAN AND TISSUE DONATION
Cross-clamp
Harvest
Collection/ transport to UMich
Tissue processing
0 min
15 min
45 min
90 min
Body
Tail
Head
Single-cell RNA sequencing
Spatial transcriptomics
Histology/multiplex IHC
B
Sex
Female n = 10
Male n = 20
Race
White n = 19
Asian n = 1
Black n = 9
Unspecified n = 1
Age distribution
Lesion n = 18
No lesion n = 12
# of Donors
Age (years)
C
100 µm

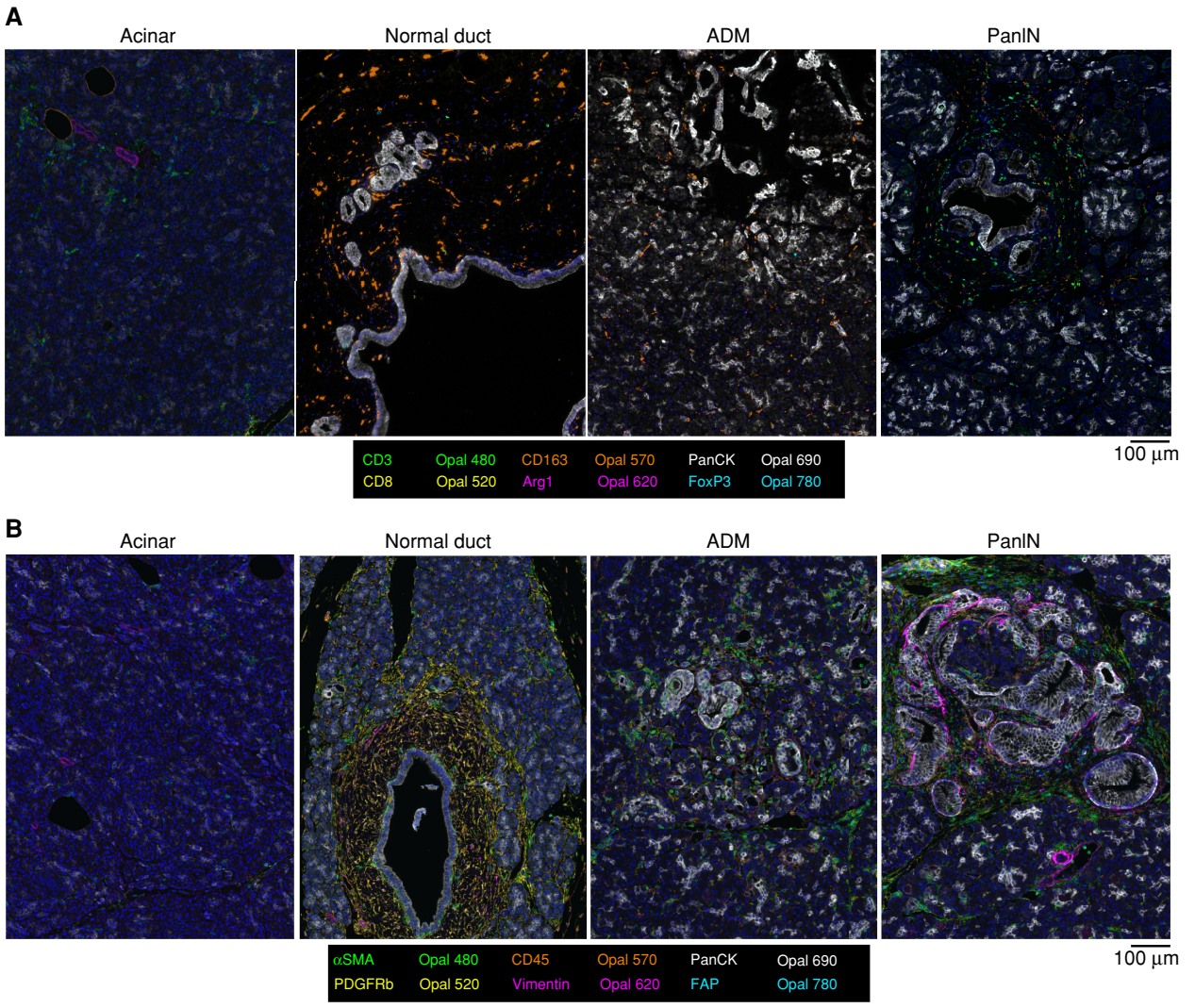

Figure 2. PanIN lesions in healthy pancreata are surrounded by a unique microenvironment. **A,** mfIHC composite images of FFPE donor tissue specimens, highlighting acinar, normal duct, ADM, and PanIN structures. Antibodies and colors of the immune panel used are in the legend below. PanCK, pancytokeratin. **B,** mfIHC composite images of FFPE donor tissue specimens, highlighting acinar, normal duct, ADM, and PanIN structures. Antibodies and colors of the fibroblast panel used are in the legend below. (*continued on following page*)

five of the pancreata, we sequenced head and tail samples separately (Supplementary Table S1, last column). On histologic analysis, four of the pancreata had PanIN lesions, whereas no lesions were detected in the remaining two. We used uniform manifold approximation and projection (UMAP) for the visualization of cell populations and identified each population based on published lineage markers, detecting epithelial cells (acini and ducts) as well as nonepithelial cells (myeloid cells, lymphocytes, fibroblasts, and endothelial cells; Fig. 3A; Supplementary Fig. S3A). The cellular composition was variable across samples, with no significant trend based on whether individual pancreata harbored lesions (Fig. 3B).

To evaluate the spectrum of myeloid populations in the human pancreas, we extracted the myeloid cells from the single-cell dataset (Fig. 3C) and identified subclusters based on previously published signatures (Supplementary Fig. S3B; ref. 23). Myeloid populations were largely dominated by alternatively activated, resident, and classical macrophages, whereas granulocytes were rare to undetectable (Fig. 3C and D). Alternatively activated macrophages expressed the expected markers of *MARCO* (scavenging receptor), *APOE*, and *SPP1*; resident macrophages were high in complement component–encoding genes; classical macrophages expressed *CCR2, LYZ,* and *FCN1;* finally, a very small population of nonclassical ($CD14^{Lo}$) macrophages expressed *FCGR3A* and *LILRA5* (Supplementary Fig. S3B and S3C).

Pancreata also harbored lymphocytes, including $CD4^+$ and $CD8^+$ T cells, B cells, and NK cells (Fig. 3E and F). We did not readily capture any Tregs. We detected both cytotoxic and exhausted $CD8^+$ T cells: the former identified by *KLRC* and *XCL1* expression, and the latter by *GZMK* and *KLRG1* expression (Supplementary Fig. S4A and S4B). Analysis of B lymphocytes showed a large population of memory B cells expressing *IGHM* and *IGHD*, germinal B cells marked by

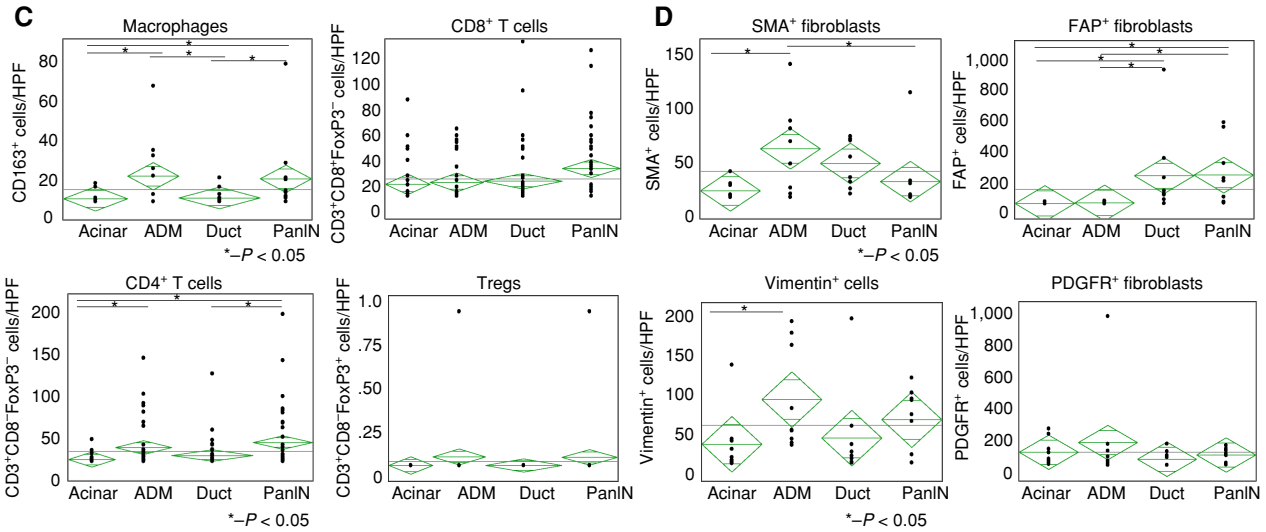

Figure 2. ***(Continued)*** **C,** Quantification of percent positive CD163$^+$ cells (top left), CD8$^+$ T cells (top right), CD4$^+$ T cells (bottom left), and Tregs (bottom right) surrounding acinar, ADM, duct, and PanIN populations, respectively. Asterisks denote a *P* value of <0.05, as determined by ANOVA. HPF, high-power field. **D,** Quantification of percent positive SMA$^+$ cells (top left), vimentin$^+$ cells (bottom left), FAP$^+$ cells (top right), and PDGFR$^+$ cells (bottom right) surrounding acinar, ADM, duct, and PanIN populations, respectively. Asterisks denote a *P* value of <0.05, as determined by ANOVA.

RGS13 expression, and plasma cells characterized by lack of *HLA-DRA* and presence of *IGHG4, SDC1,* and *IGHG1* (Supplementary Fig. S4A and S4C).

Thus, the human pancreas houses a variety of innate and adaptive immune cells. Of note, the dissociation step, required for single-cell RNA sequencing, precludes the determination of whether any of the immune cells were derived from normal pancreas parenchyma or from areas surrounding PanIN lesions; however, our multiplex immunostaining data show that macrophages are present throughout the tissue, whereas T cells are more likely to localize near PanIN (Fig. 2).

We then analyzed fibroblasts, endothelial cells, and pericytes together, as these cells share several markers. We identified three distinct populations of fibroblasts: Fibro1 (*DPT* low), Fibro2 (*DPT* high), and Fibro3 (expressing *FBLN2* and *CFD*; Fig. 3G and H; Supplementary Fig. S5A). Notably, *DPT* was recently described as a pan-fibroblast marker across multiple organs and disease states in mouse tissues (40); based on our data, *DPT* is expressed across fibroblast populations in the adult human pancreas, albeit at variable levels (Supplementary Fig. S5B). Fibroblasts also had universally high expression of *PDGFRB/A* and, to a lesser extent, *PDPN* (Supplementary Fig. S5B and S5C). *PDGFRB* was also expressed by pericytes, whereas *PDGFRA* was expressed only in fibroblasts (Supplementary Fig. S5B and S5C). In contrast, *ACTA2* was expressed by only a small subset of fibroblasts (Supplementary Fig. S5B). *LRRC15*, a marker recently associated with tumor-promoting pancreatic cancer-associated fibroblasts (CAF; ref. 41), was not expressed in normal pancreas fibroblasts, but was detected in a few cells in the Endo5 endothelial cell cluster (Supplementary Fig. S5B). Lastly, FABP4, which labels pancreatic stellate cells in mice (42), labeled only a few fibroblasts but was widely expressed by pericytes and endothelial cells, possibly highlighting a mouse/human difference or reflecting the age of the donors (Supplementary Fig. S5B). We then compared our fibroblast populations with fibroblasts described in the healthy mouse pancreas (41, 43). We did not observe a 1:1 correlation between any of those previously described mouse populations and our human fibroblast populations, but, broadly, the mouse gene signatures were expressed in human fibroblasts, highlighting some common aspects but also possible species-specific differences (Supplementary Fig. S5D). We identified five endothelial cell populations (Endo1–5; Fig. 3G and H; Supplementary Fig. S5A and S5E), expressing varying levels of *VWF, CDH5, FABP5*, and *CD74* (Supplementary Fig. S5A), and two pericyte populations, expressing RGS5 (Supplementary Fig. S5A). The Endo5 population was notable given its elevated expression of angiogenic factors *IL33, TFF3, CXCL2,* and *KRT18* (Supplementary Fig. S5A and S5E). The prevalence of each cell type, both for immune and nonimmune components of the microenvironment, was variable across donor samples.

Overall, the normal pancreas includes a heterogeneous set of structural cells, such as fibroblasts, pericytes, and endothelial cells, as well as immune cells. The normal human pancreas also presents with histologic heterogeneity, reflecting age and the complexities of human lifestyle and genetics.

Comparison of the Microenvironment in Healthy Pancreata and Pancreatic Tumors Reveals Distinct Stromal Features

We next sought to investigate the differences in the microenvironment of the normal pancreas and pancreatic cancer. For this purpose, we integrated single-cell RNA sequencing data from healthy donor samples (6 pancreata; 11 samples total) with our previously published dataset (24) of tumor (n = 16) and adjacent normal (n = 3) samples. The latter were obtained from patients undergoing surgery for duodenal adenoma, ampullary carcinoma, or PDAC, respectively,

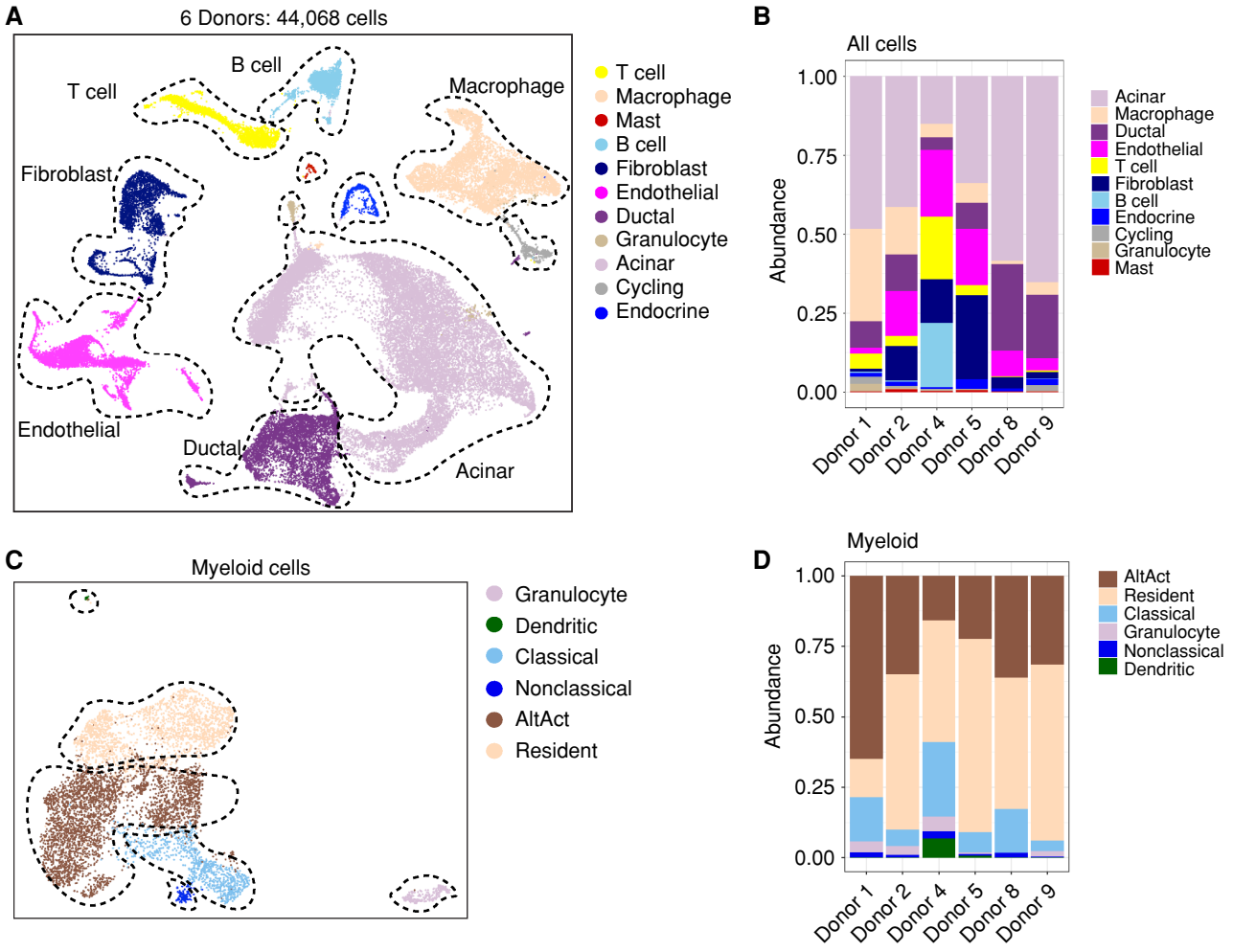

Figure 3. Healthy pancreata contain several nonepithelial populations, including myeloid cells, lymphocytes, fibroblasts, and endothelial cells. **A,** UMAP of all cells captured from single-cell RNA sequencing of six donor pancreata. Populations are identified by color. **B,** Histogram of cell-type abundance of all captured cells by donor. **C,** UMAP of extracted myeloid cells from donor pancreata. Populations are identified by color. AltAct, alternatively activated macrophages. **D,** Histogram of cell-type abundance of specific myeloid cell populations by the donor. (*continued on following page*)

and tissue was confirmed to be free of cancer by pathologic evaluation. UMAP two-dimensional visualization showed a wide variety of epithelial and nonepithelial cells (Fig. 4A). In terms of cell-type composition, each sample was unique (Supplementary Fig. S6A); however, some common themes emerged. As expected, acinar cells were captured in abundance in the normal samples and, to an extent, in adjacent normal, whereas they were rarely captured in tumor samples (Fig. 4B; Supplementary Fig. S6B). Conversely, tumor samples had a higher proportion of macrophages and $CD4^+$ T cells. Granulocytes were rarely detected in normal samples and observed in only one of three adjacent normal samples, but they were abundant in most tumor samples. The proportion of $CD8^+$ T cells was variable across each group of samples. Endothelial cells were generally more abundant in healthy pancreata and adjacent normal, although occasionally detected in individual tumors. Using differential abundance analysis to generate a neighborhood graph differential abundance plot (44) between healthy and tumor samples, we defined cell populations with significant shifts in abundance between tumor and normal states (Fig. 4C). We generated a beeswarm differential abundance plot (44) and found that across all samples, comparing tumors versus normal showed loss of acinar cells and endothelial cells, and an increase in myeloid cells and nonacinar epithelial cells, likely cancer cells, in the tumor samples (Fig. 4D).

To determine whether gene expression alone could distinguish between tumor samples and normal pancreas, we aggregated sequencing data from all of the cells in each sample (pseudobulk) and applied correlation and principal component analysis (PCA) on normalized gene–sample count matrices. Both plots showed that tumor samples largely clustered separately from healthy samples; adjacent normal samples were variable (Fig. 4E and F). The classification of adjacent normal is to be interpreted with caution given the relatively small sample size. As the pseudobulk analysis of total cells is affected by cellular composition in each sample, we then repeated the analysis on a population-specific basis, initially

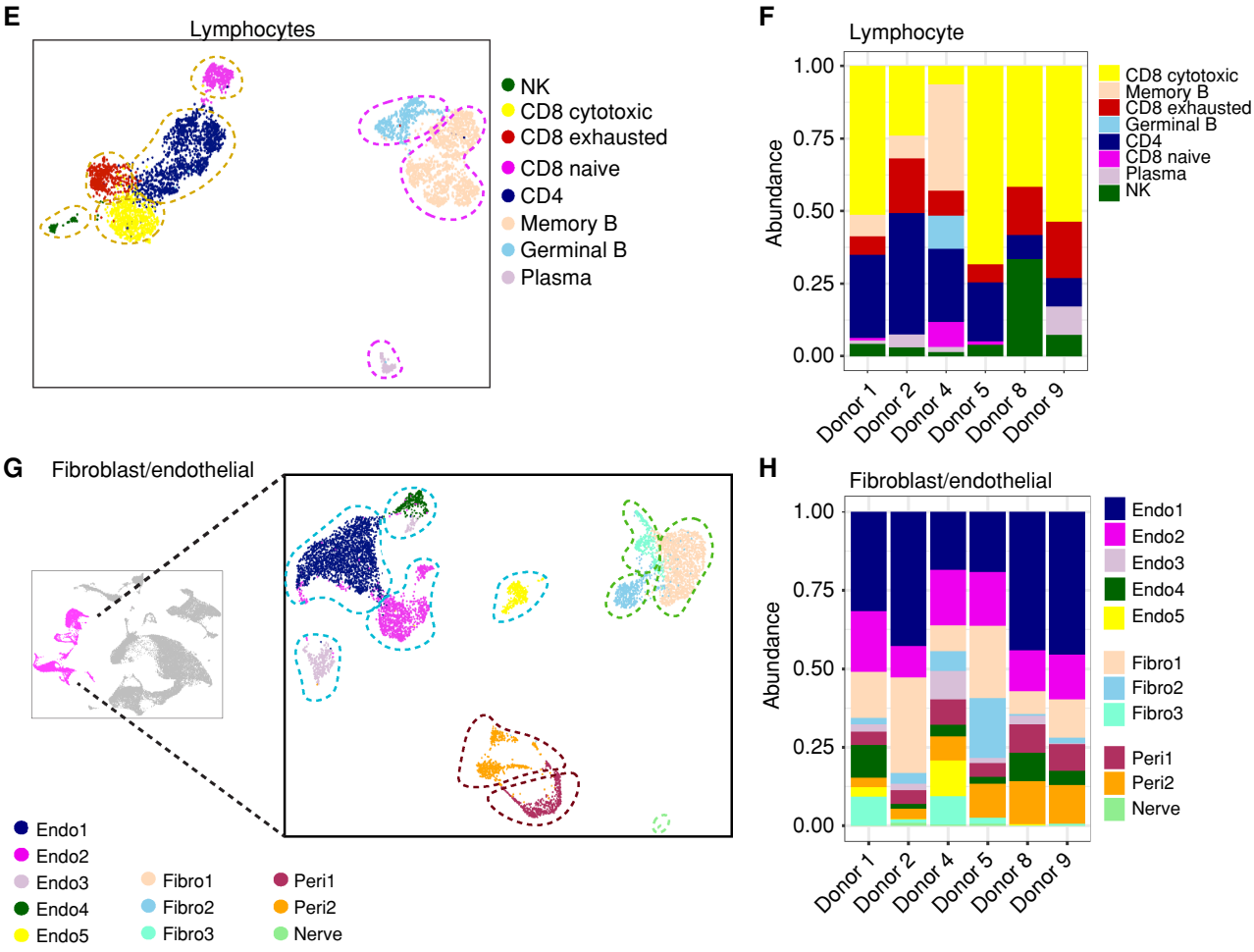

Figure 3. ***(Continued)*** **E,** UMAP of extracted lymphocytes from donor pancreata. Populations are identified by color. **F,** Histogram of cell-type abundance of specific lymphocyte populations by donor. **G,** UMAP of extracted fibroblast, pericyte, and endothelial populations from donor pancreata. Populations are identified by color. **H,** Histogram of cell-type abundance of specific fibroblast, pericyte, and endothelial populations by donor.

focusing on broad stromal cell populations, namely, myeloid cells, T cells, and fibroblasts. The PCA plots revealed clear clustering of tumor versus normal samples, whereas adjacent normal were variable and at times interspersed with the healthy and/or tumor samples (Fig. 4F). Lastly, we plotted predicted ligand–receptor interactions (45) between cell populations that were increased in tumors compared with normal samples (Supplementary Table S2). Epithelial signals enriched in tumor samples included *EGFR* ligands, consistent with the activation of this pathway in pancreatic cancer (46, 47). *SAA1*, a factor linked to the promotion of pancreatic carcinogenesis (48), was also elevated in tumors (Fig. 4G). Signaling from fibroblasts (as well as from pericytes and endothelial cells) was prominently increased in tumor samples when all possible interactions were measured (Supplementary Fig. S6C and S6D); specific findings include an increase in extracellular matrix signaling driven by collagen and fibronectin (Fig. 4G), consistent with the fibrotic microenvironment of pancreatic cancer (49). Macrophages showed an increased production of *CCL* and *CXCL* family cytokines linked to tumor-promoting and immunosuppressive pathways (50, 51).

To further investigate changes in cellular composition and gene expression patterns, we further analyzed specific cell populations. For this comparison, we focused on myeloid cells and fibroblasts—cell types that were present in abundance in both tumor and normal samples. Myeloid cells included granulocytes, derived largely from tumors, and several populations of macrophages detected across samples (Fig. 5A; Supplementary Fig. S7A). Dendritic cells (including FCER1A$^+$, CLEC9A$^+$, and LAMP3$^+$ dendritic cells) were detected in a few of the samples, but were not abundant enough for meaningful gene expression comparisons. In contrast, alternatively activated, classical, nonclassical, and resident macrophages (defined based on the markers shown in Supplementary Fig. S7B) were abundant both in the healthy pancreas and in pancreatic cancer. PCA of each of these populations revealed distinct gene expression patterns in tumors versus healthy organs; adjacent normal samples were again variable and interspersed with healthy and tumor samples (Fig. 5B). Pathway annotation revealed an increase in chemotaxis pathways in tumors versus healthy pancreata, indicating that signaling programs in myeloid migration are largely responsible for the transcriptomic

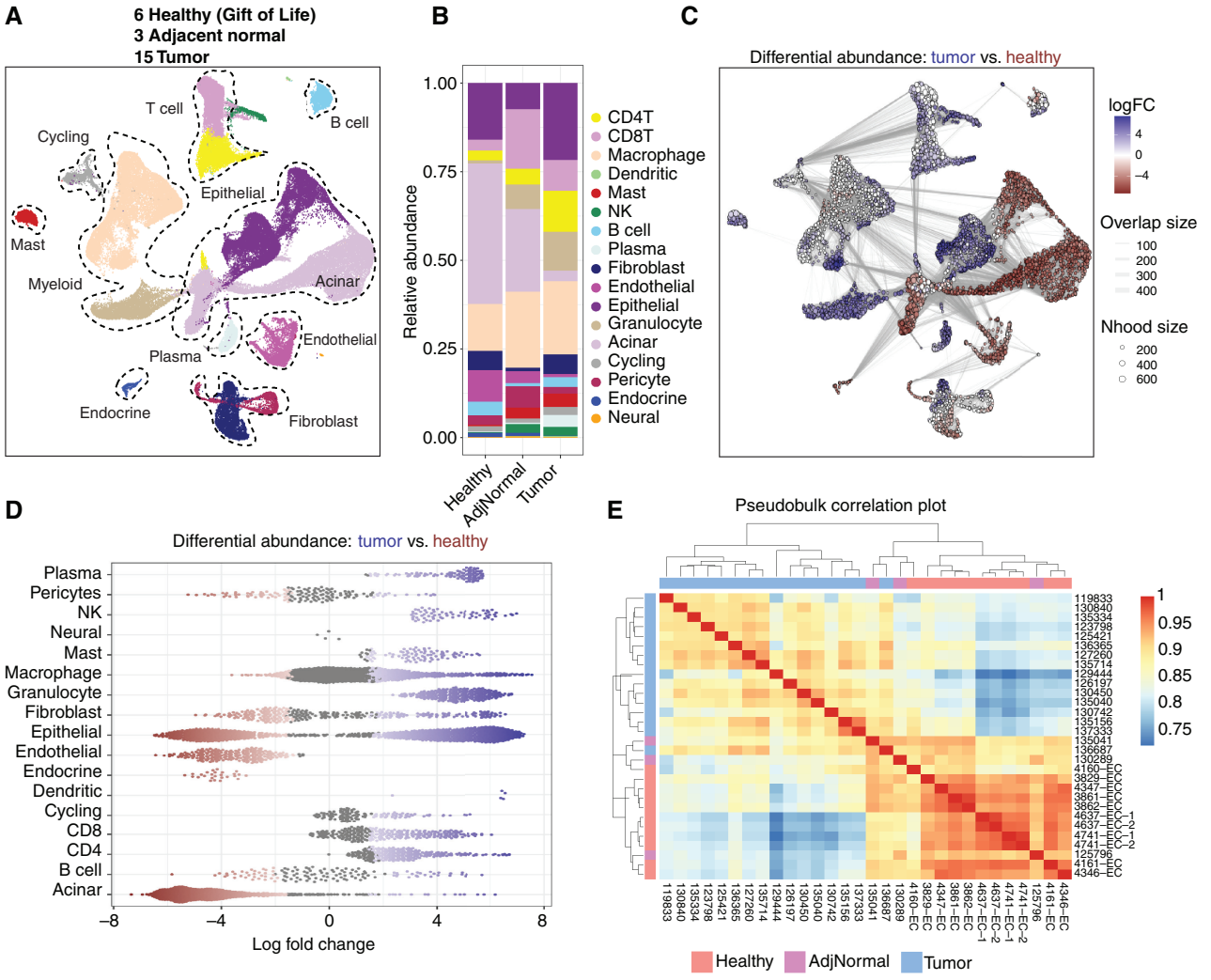

Figure 4. Comparison of the microenvironment in healthy pancreata and pancreatic tumors reveals distinct stromal features. **A,** UMAP of all cells captured from single-cell RNA sequencing of six donor pancreata merged with 15 PDAC samples and 3 adjacent normal samples. Populations are identified by color. **B,** Histogram of cell-type abundance of all cell populations by disease state [healthy, adjacent normal (AdjNormal), and tumor]. **C,** Neighborhood graph differential abundance plot of the merged tumor, healthy, and adjacent normal samples. Size of dots represents neighborhoods, whereas edges represent the number of cells shared between neighborhoods. Neighborhoods colored in red represent significantly increased abundance in healthy samples, whereas neighborhoods colored in blue represent significantly increased abundance in tumor samples. logFC, log-fold change; Nhood, neighborhood. **D,** Beeswarm plot of differential abundance by cell type. *X*-axis represents a log-fold change in abundance between tumor and healthy states. Each dot is a neighborhood; neighborhoods colored in red represent significantly increased abundance in healthy samples, whereas neighborhoods colored in blue represent significantly increased abundance in tumor samples. **E,** Correlation heat map of pseudobulk-aggregated counts of 15 tumor samples, 3 adjacent normal samples, and 11 donor samples (given that single-cell sequencing was performed on the head and tail sections separately in 5 out of 6 donors). Each row/line represents one aggregated single-cell sequencing sample. (*continued on following page*)

differences between tumor and healthy states (Supplementary Fig. S7C). Performing differential expression analysis between macrophages from the healthy organs versus tumors interestingly did not reveal any signature markers of tumor-associated macrophages (TAM; ref. 52; Fig. 5C). We then individually plotted known TAM markers. Among those, *APOE, MRC1, C1QA, C1QB,* and *SPP1,* described by our group and others as TAM-specific in mouse models (52–54), were unexpectedly expressed at similar levels in healthy pancreas–associated macrophages and TAMs (Fig. 5D). The only exception was *CXCL8,* which was detected only in TAMs (Fig. 5C and D). This finding was surprising and differentiated our human data from mouse model findings, in which these factors are lowly expressed or undetectable in healthy organ macrophages.

Fibroblast and pericyte clustering identified two distinct fibroblast and two distinct pericyte populations (Fig. 5E and F; Supplementary Fig. S7D and S7E). Fibroblast cluster Fibro2 was almost entirely derived from tumor samples, whereas fibroblast cluster Fibro1 was derived from both healthy and tumor samples but predominantly the former. Interestingly, fibroblast cluster Fibro2 expressed relatively high levels of the myofibroblastic CAF (myCAF; ref. 23) marker *ACTA2* and decreased expression of the inflammatory CAF (iCAF; ref. 23) marker *CXCL12*, in addition to increased expression of FAP (a CAF marker known to mediate immunosuppression; ref. 55) and exclusive expression of CD55 and LRRC15. These data show that healthy pancreas fibroblasts are altogether distinct from CAFs, a notion supported by

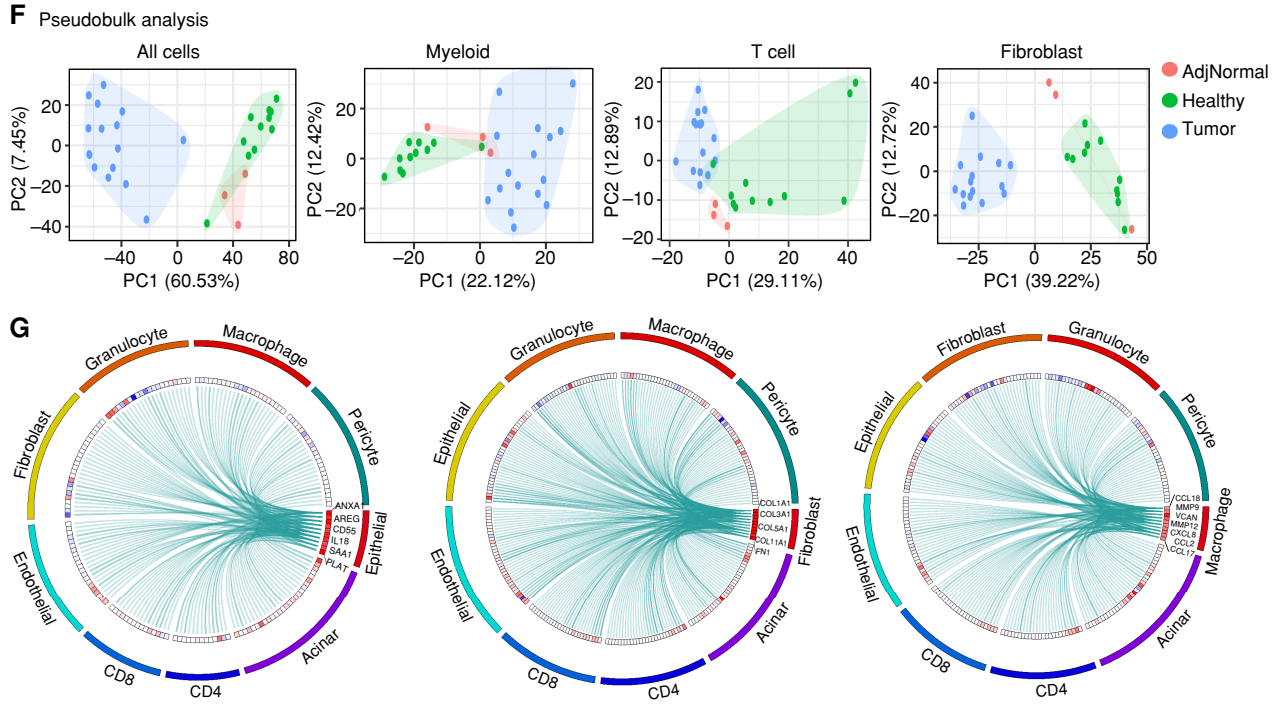

Figure 4. ***(Continued)*** **F,** PCA plots of pseudobulk-aggregated counts from all cells, myeloid cells, T cells, and fibroblasts. Each dot represents one aggregated single-cell sequencing sample. **G,** Circos plots of putative ligand–receptor interactions that are upregulated in PDAC epithelial cells (left), fibroblasts (middle), and macrophages (right) compared with healthy cells. The heat map within the circos plots is the scaled average expression of each gene within PDAC tissue cell populations. The interactions plotted are those in which the expression level of the ligand is increased in PDAC samples compared with healthy tissues.

distinct clustering on PCA (Fig. 5G). Differential expression analysis again revealed an increase in activation markers and markers of tumor-promoting fibroblasts in tumor samples, such as ACTA2, FAP, and LRRC15 (Fig. 5H shows the top 20 differentially expressed genes; Fig. 5I shows selected additional fibroblast-specific genes).

Of note, we also captured several lymphocyte and NK populations, although this group was mostly derived from tumor samples, with the exception of naive T cells, which were largely detected in healthy organs (Supplementary Fig. S8A and S8B). PCA plots revealed a spectrum, with some tumor T cells clustering within the normal T-cell populations, and others quite distinct (Supplementary Fig. S8C); pathway analysis showed tumor samples were enriched for genes in negative regulation of T-cell proliferation (Supplementary Fig. S8D). However, overall these T cells were less distinct between tumor and normal, an interesting finding given the hallmarks of poor immunogenicity, immune exhaustion, and impaired cytotoxic activity of T cells in pancreatic cancer (24, 56).

Overall, our analysis of human pancreata shows frequent PanINs in organs of healthy individuals. Comparison with PanINs with tumors samples identified shared inflammatory gene expression profiles of macrophages. In contrast, fibroblasts were clearly divergent in tumors compared with PanIN. Finally, T cells were rare to undetectable in normal areas of the pancreas, present in small numbers in PanINs and common in pancreatic cancer, although subsets such as Tregs were almost uniquely present only in tumors. Thus, comparative analysis reveals both similarities and differences in the components of the microenvironment.

Spatial Transcriptomics Reveals a Unique Epithelial Gene Signature of PanIN Lesions That Aligns Closely with Tumor Epithelium

We next focused on the epithelial population in our single-cell RNA sequencing dataset to determine if we could identify transitory cell populations, including cells undergoing ADM and cells from PanIN lesions. Analysis of the epithelial and acinar populations revealed 16 distinct subclusters (Supplementary Fig. S9A and S9B), with clusters 4, 5, and 6 derived mainly from tumor samples (Supplementary Fig. S9C). These clusters had high expression of *S100* genes, encoding for a family of proteins often elevated in cancer cells (57) and linked to pancreatic cancer metastasis (ref. 58; Supplementary Fig. S9D). In the quest to identify any PanIN cells in donor samples, we investigated previously reported transcriptomic signatures specific to acinar, ductal, PanIN, and cancer cells (59) in our sequencing data. Using enrichment analysis, we defined clusters enriched for the acinar, ductal, and cancer cell signatures. As expected, the acinar signature marked cells largely derived from healthy and adjacent normal samples, whereas tumor signature marked cells from PDAC samples (Supplementary Fig. S9E). We also identified cell populations enriched for the previously described Duct-like1 (expressing normal ductal genes) and Duct-like2 (with increased expression of mucus and trefoil factor genes) signatures. In our dataset, the former mapped to cells from

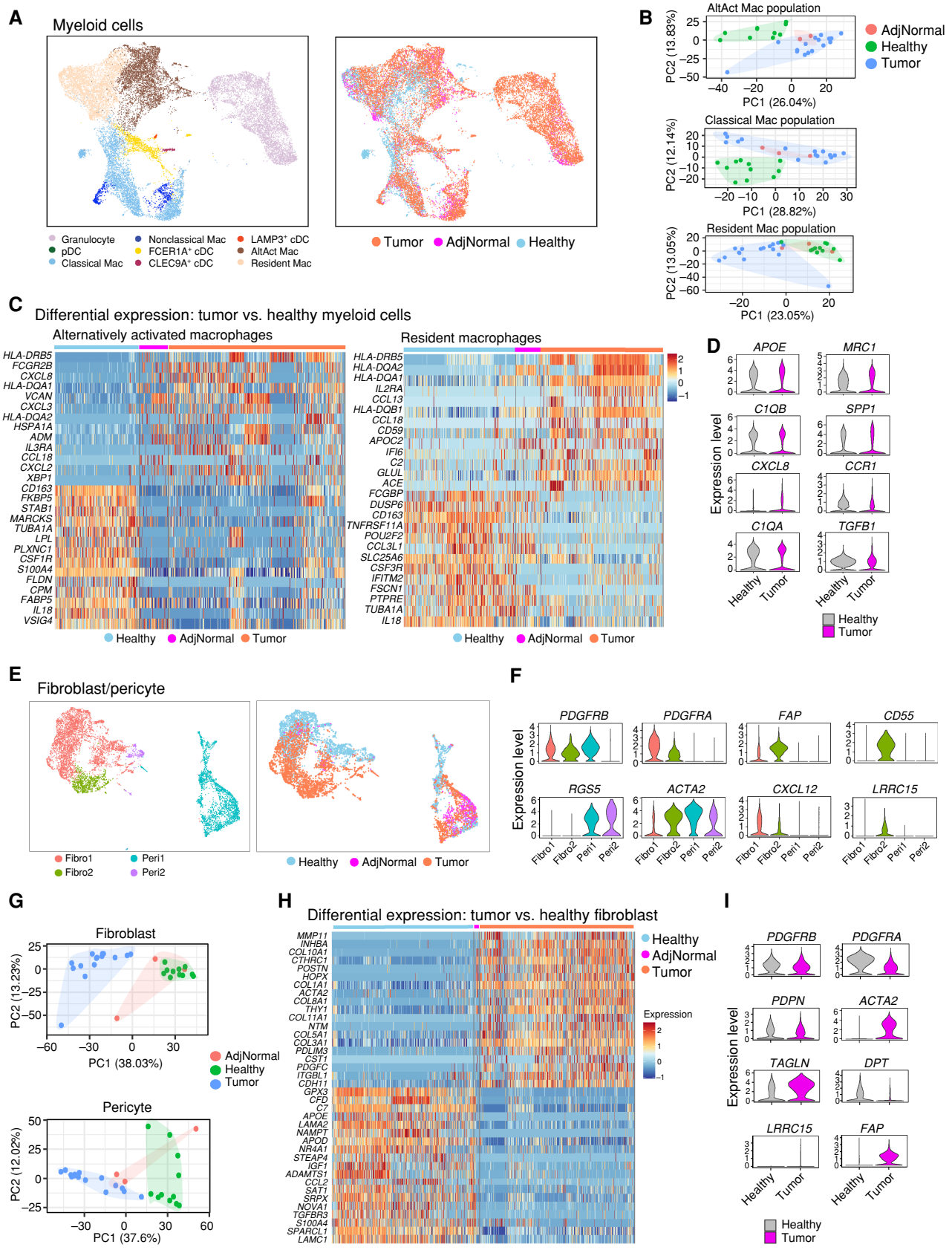
A
Myeloid cells
Granulocyte
pDC
Classical Mac
Nonclassical Mac
FCER1A+ cDC
CLEC9A+ cDC
LAMP3+ cDC
AltAct Mac
Resident Mac
Tumor
AdjNormal
Healthy
B
AltAct Mac population
PC2 (13.83%)
PC1 (26.04%)
Classical Mac population
PC2 (12.14%)
PC1 (28.82%)
Resident Mac population
PC2 (13.05%)
PC1 (23.05%)
AdjNormal
Healthy
Tumor
C
Differential expression: tumor vs. healthy myeloid cells
Alternatively activated macrophages
HLA-DRB5
FCGR2B
CXCL8
HLA-DQA1
VCAN
CXCL3
HLA-DQA2
HSPA1A
ADM
IL3RA
CCL18
CXCL2
XBP1
CD163
FKBP5
STAB1
MARCKS
TUBA1A
LPL
PLXNC1
CSF1R
S100A4
FLDN
CPM
FABP5
IL18
VSIG4
Resident macrophages
HLA-DRB5
HLA-DQA2
HLA-DQA1
IL2RA
CCL13
HLA-DQB1
CCL18
CD59
APOC2
IFI6
C2
GLUL
ACE
FCGBP
DUSP6
CD163
TNFRSF11A
POU2F2
CCL3L1
SLC25A6
CSF3R
IFITM2
FSCN1
PTPRE
TUBA1A
IL18
Healthy
AdjNormal
Tumor
D
APOE
MRC1
C1QB
SPP1
CXCL8
CCR1
C1QA
TGFB1
Expression level
Healthy
Tumor
E
Fibroblast/pericyte
Fibro1
Fibro2
Peri1
Peri2
Healthy
AdjNormal
Tumor
F
PDGFRB
PDGFRA
FAP
CD55
RGS5
ACTA2
CXCL12
LRRC15
Expression level
Fibro1
Fibro2
Peri1
Peri2
G
Fibroblast
PC2 (13.23%)
PC1 (38.03%)
Pericyte
PC2 (12.02%)
PC1 (37.6%)
AdjNormal
Healthy
Tumor
H
Differential expression: tumor vs. healthy fibroblast
MMP11
INHBA
COL10A1
CTHRC1
POSTN
HOPX
COL1A1
ACTA2
COL8A1
THY1
COL11A1
NTM
COL5A1
COL3A1
PDLIM3
CST1
PDGFC
ITGBL1
CDH11
GPX3
CFD
C7
APOE
LAMA2
NAMPT
APOD
NR4A1
STEAP4
IGF1
ADAMTS1
CCL2
SAT1
SRPX
NOVA1
TGFBR3
S100A4
SPARCL1
LAMC1
Healthy
AdjNormal
Tumor
Expression
I
PDGFRB
PDGFRA
PDPN
ACTA2
TAGLN
DPT
LRRC15
FAP
Expression level
Healthy
Tumor

normal and adjacent normal samples, with the latter mapping within tumor-derived cells (Supplementary Fig. S9E). In contrast, we were unable to map the PanIN signature in our single-cell dataset (Supplementary Fig. S9E). Interestingly, utilizing genes for *HALLMARK_KRAS_SIGNALING_UP* and *_DOWN* (60), we observed that tumor-derived epithelial cells were relatively enriched for genes upregulated with KRAS activation and relatively depleted from genes downregulated with KRAS activation (Supplementary Fig. S9F). We hypothesized that PanIN cells, a relatively rare population, were not captured in our single-cell dataset; another possibility is that the PanIN signature derived from tumor-adjacent PanIN, as in previous studies (59), is distinct from sporadic PanIN in healthy pancreata.

To directly evaluate the gene expression pattern of PanIN, we utilized the GeoMx NanoString spatial transcriptomics platform. After careful review of tissue slides with a clinical pathologist (J. Shi, who specializes in pancreatic histopathology), acinar, normal duct, ADM, and PanIN regions of interest (ROI) were selected from the donor pancreata, whereas tumor-associated PanIN, glandular tumor, and poorly differentiated tumor ROIs were selected from malignant samples (Fig. 6A and B). In addition, we collected ROIs from acini and normal ducts adjacent to tumors for comparison. To avoid confounding transcripts from the stroma, samples from each region were segmented using pancytokeratin (PanCK) and CD45 to select $PanCK^+/CD45^-$ cells in all ROIs, with the exception of acinar ROIs, where we selected $PanCK^-/CD45^-$ (as acinar cells do not express PanCK and can be easily identified histologically). Following quality control and data normalization, we performed PCA and detected a prominent batch effect. Upon correction, we obtained acinar and PanIN ROIs that clustered separately, whereas ADM and normal duct ROIs were interspersed with each other, indicating transcriptional similarity, which is expected (Supplementary Fig. S10A). To extract gene signatures specific to each cell type, we applied linear mixed-model differential expression analysis comparing each cell type to all other remaining cell types (Supplementary Fig. S10B; Fig. 6C; Supplementary Table S3). We thus identified expected digestive enzymes in acinar ROIs (*CEL, CPA1, CELA2B,* and *PRSS3*) and genes encoding for mucins in ductal ROIs (*MUC5B* and *MUC20*). Ductal ROIs also expressed *AQP3*, encoding for a water channel protein typically found on the basolateral membrane of ducts (61); *MUC5B*, expressed in the noncancerous pancreatic ductal epithelium (62); and *MUC20*, expression of which has not been previously reported in the pancreas. PanIN ROIs were enriched for the previously described marker *CLDN18* (59, 63). We also detected expression of trefoil factor genes *TFF1* and *TFF2*. TFF1/2 are small secreted proteins that are expressed in PanINs and, to a lesser degree, in early PDAC (64, 65). Interestingly, *MUC5AC*, a known PanIN marker (66), was not specifically enriched in PanIN, as its expression was also higher in glandular tumors and ducts (Supplementary Fig. S10C). ADM ROIs included *AQP1* (in contrast to normal ducts marked by *AQP3*), as well as serpin family genes (*SERPING1*) and complement (*C6*)—an interesting combination, as serpins regulate the complement cascade (67). Although the complement system has been implicated in the pathogenesis of pancreatic cancer (53, 68), this is the first report of its upregulation in ADM from a healthy pancreas, suggesting that complement dysregulation may be an early preneoplastic event. Lastly, glandular and poorly differentiated tumor ROIs were distinct, with glandular tumors more similar to PanIN, as expected. Although healthy samples and tumor-bearing samples had a high degree of concordance in marker features for acinar, ductal, and PanIN marker features (as ADM was captured only in healthy samples), we noted that PanINs from tumor-bearing samples had higher expression of genes seen commonly in tumor ROIs, suggesting a closer association with malignancy.

Using gene set variation analysis (GSVA), we investigated the enrichment of the previously reported PDAC subtype–specific signatures (69–71). Although acinar and ADM ROIs showed relative enrichment of ADEX and exocrine-like subtype signatures, PanIN ROIs were enriched to classical signature, and the poorly differentiated tumor ROIs displayed basal signature enrichment. Interestingly, PanIN ROIs corresponded more closely to the classical signature than glandular tumors, as the latter showed expression of basal-like genes as well, consistent with recent reports on intermediary states between classical and basal in most human tumors at the single-cell level (refs. 26, 72; Supplementary Fig. S10D). In concordance with our prior differential expression analysis showing differences between PanINs from different sources (Fig. 6C), PanINs from tumor-bearing samples expressed some basal-like genes, whereas PanINs from healthy samples did not. Thus, sporadic PanINs from otherwise healthy pancreata are similar to but distinct from tumor-adjacent PanINs.

We then integrated spatial transcriptomics with single-cell RNA sequencing data. Using the top 20 genes from each ROI class, we defined cell type–specific gene signatures for acinar, ductal, ADM, PanIN, and tumor cells and mapped these signatures to the epithelial cluster from the single-cell

Figure 5. Myeloid and fibroblast populations from tumor-bearing pancreata display distinct transcriptomic signatures compared with their nontumor counterparts. **A,** Left, UMAP of extracted myeloid cells from the single-cell dataset of healthy, adjacent normal, and tumor samples. Populations are identified by color. Right, UMAP overlay of disease states on extracted myeloid cells from the single-cell dataset of healthy, adjacent normal, and tumor samples. AdjNorm, adjacent normal; AltAct, alternatively activated macrophages; cDC, conventional dendritic cells; pDC, plasmacytoid dendritic cells; Mac, macrophage. **B,** PCA plots of pseudobulk-aggregated counts from specific myeloid cell populations. Each dot represents one aggregated single-cell sequencing sample. **C,** Top differentially expressed genes between alternatively activated macrophages (left) and resident macrophages (right) from healthy (blue) and tumor (orange) samples. **D,** Violin plots of normalized expression of select TAM markers comparing healthy to tumor samples. Adjusted *P* value for significantly differentially expressed markers: *CXCL8* 4.64E-59. **E,** Left, UMAP of extracted fibroblast and pericyte cells from the single-cell dataset of healthy, adjacent normal, and tumor samples. Populations are identified by color. Right, UMAP overlay of disease states on extracted fibroblast/pericyte cells from the single-cell dataset of healthy, adjacent normal, and tumor samples. **F,** Violin plots of normalized expression of select fibroblast markers mapped across fibroblast and pericyte populations. Adjusted *P* value for significantly differentially expressed markers: *PDGFRA* 1.58E-308, *ACTA2* 1.85E-261, *TAGLN* 1.18E-117, *DPT* 2.00E-67, and *FAP* 3.63E-308. **G,** PCA plots of pseudobulk-aggregated counts from fibroblast (top) and pericyte (bottom) populations. Each dot represents one aggregated single-cell sequencing sample. **H,** Top differentially expressed genes between fibroblasts from healthy (blue) and tumor (orange) samples. **I,** Violin plots of normalized expression of select fibroblast markers comparing healthy to tumor samples.

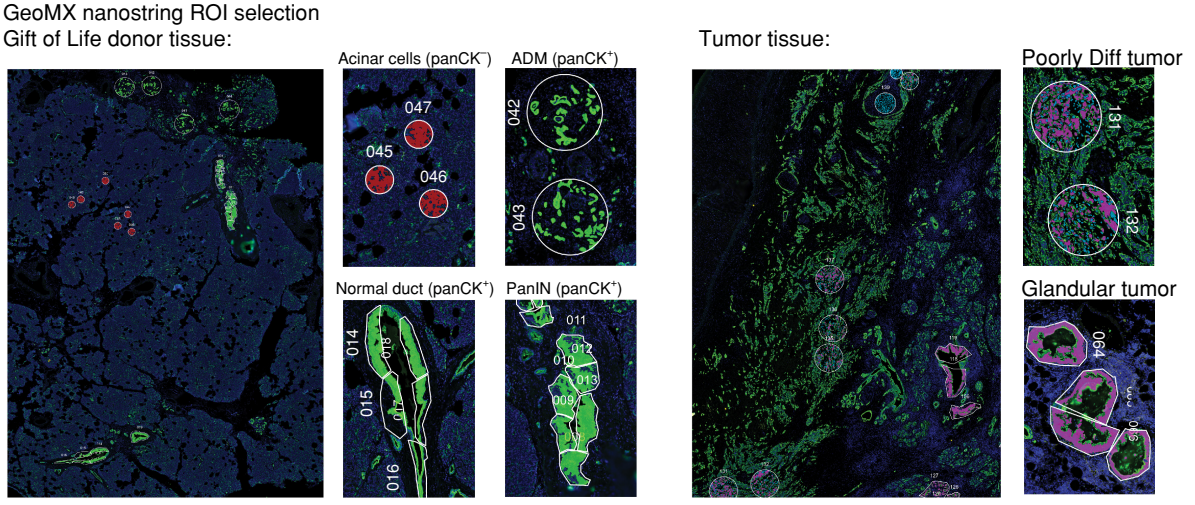
A
GeoMX nanostring ROI selection
Gift of Life donor tissue:
Acinar cells (panCK⁻)
ADM (panCK⁺)
Normal duct (panCK⁺)
PanIN (panCK⁺)
Tumor tissue:
Poorly Diff tumor
Glandular tumor

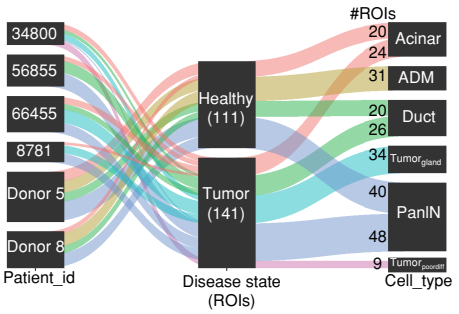
B
#ROIs
34800
56855
66455
8781
Donor 5
Donor 8
Patient_id
Healthy (111)
Tumor (141)
Disease state (ROIs)
Acinar
ADM
Duct
PanIN
Cell_type

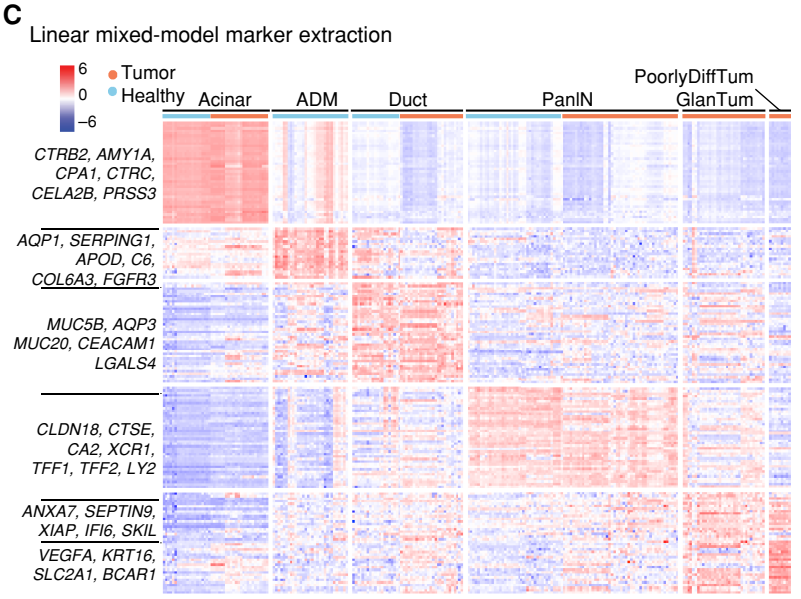
C
Linear mixed-model marker extraction
Tumor
Healthy
Acinar
ADM
Duct
PanIN
PoorlyDiffTum
GlanTum
CTRB2, AMY1A, CPA1, CTRC, CELA2B, PRSS3
AQP1, SERPING1, APOD, C6, COL6A3, FGFR3
MUC5B, AQP3 MUC20, CEACAM1 LGALS4
CLDN18, CTSE, CA2, XCR1, TFF1, TFF2, LY2
ANXA7, SEPTIN9, XIAP, IFI6, SKIL
VEGFA, KRT16, SLC2A1, BCAR1

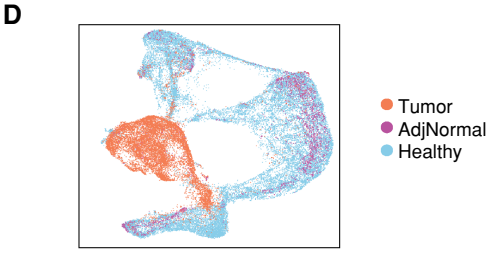
D
Tumor
AdjNormal
Healthy

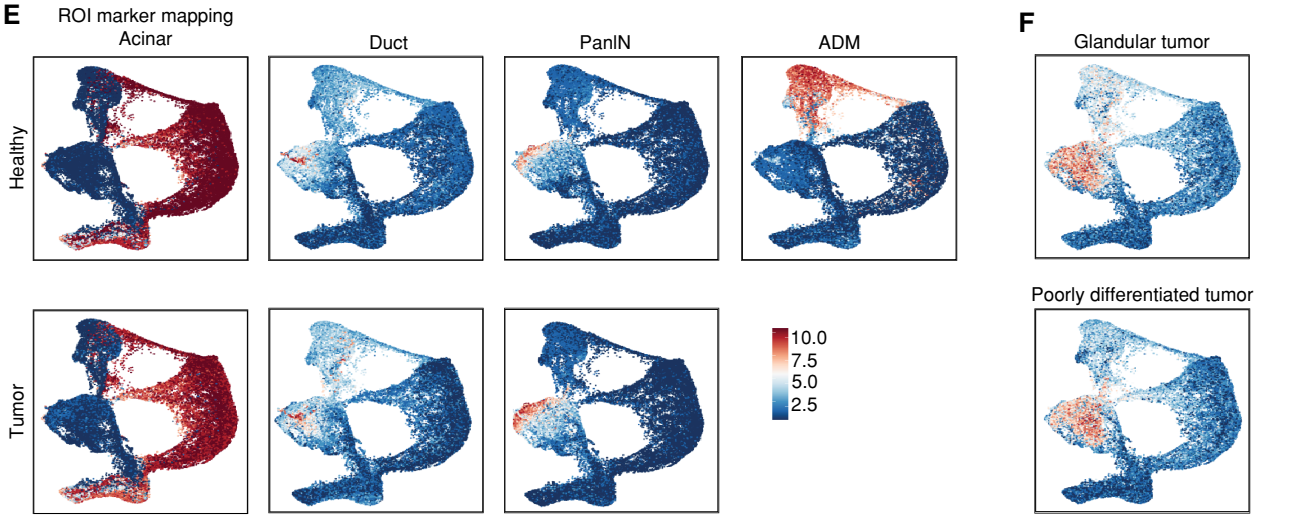
E
ROI marker mapping
Acinar
Duct
PanIN
ADM
Healthy
Tumor
10.0
7.5
5.0
2.5
F
Glandular tumor
Poorly differentiated tumor

epithelial sequencing data (Fig. 6D–F). Our aim was to map cell populations relatively enriched for each defined signature. As expected, the spatial transcriptomic–derived signatures identified distinct acinar, ADM, and ductal populations (Fig. 6E). The glandular and poorly differentiated tumor signatures were, as expected, enriched in cells derived from tumor samples (Fig. 6F). Although the glandular tumor signature mapped to cells spanning most of the epithelial population, consistent with its heterogeneous subtype scoring, the poorly differentiated tumor signature was confined to tumor-derived epithelial cells. Interestingly, the ADM signature was enriched in the donor-derived epithelial cells, whereas the PanIN and normal ductal signatures from both healthy and tumor-bearing samples mapped only to specific clusters derived from tumor samples, an unexpected finding. We thus queried whether these lesions harbored mutations in the *KRAS* gene, as previously described in human tumor-associated PanIN (73). Droplet PCR analysis revealed the presence of multiple *KRAS* mutations in the samples queried (Supplementary Table S4), a finding that concords with the described polyclonality of PanINs with associated distinct KRAS mutational profiles (bioRxiv 2023.01.27.525553).

PanINs from tumors notably marked a slightly larger population of cells within the tumor-derived epithelial population than PanINs from healthy samples. This supported the differential expression analysis, which showed more shared features of tumor-bearing PanIN ROIs with tumor ROIs, compared with PanINs from healthy samples. Overall, although differences between cancer cells, tumor-associated PanINs, and sporadic PanINs from healthy organs existed, similarities far outweighed any difference, suggesting that these neoplastic lesions have already acquired many, albeit not all, features of malignant cells.

Claudin 18, MUC5AC/B, and AQP1/3 Distinguish Normal Ducts, ADM, and PanIN in Healthy Pancreas

We next endeavored to validate our gene signatures in donor tissue to determine whether they accurately identified different epithelial populations, as suggested by our transcriptomic data. We selected markers that distinguished each epithelial cell type (Fig. 6C). Our list included AQP1 (ADM-specific), MUC5B and AQP3 (normal duct–specific), and CLDN18 and an *in situ* hybridization probe for *TFF1* (PanIN-specific), for which antibodies were readily available. We included MUC5AC as a PanIN marker, as our data support its exclusive expression in PanINs in nontumor-bearing samples (compared with normal ducts, ADM, and acinar cells; Supplementary Fig. S10C). For each of these markers, we performed coimmunofluorescent staining on sections obtained from four different donor pancreata, including E-Cadherin as a common epithelial lineage marker (Supplementary Figs. S11–S14). We also stained for p-ERK to assess the status of ERK activation in normal pancreas within acinar cells, ADM, normal ducts, and PanINs. In sections containing both PanIN and normal ducts, MUC5B stained only normal ducts, whereas MUC5AC was specific for PanIN (Fig. 7A and B). CLDN18 staining was elevated in PanIN but also was positive in ADM to a lesser degree (Fig. 7C). AQP3 stained only normal ducts, whereas AQP1 was specific to ADM (Fig. 7D and E). *TFF1* was coexpressed with CLDN18 in PanIN (Fig. 7F). Lastly, PanIN lesions expressed high levels of p-ERK, whereas areas of ADM were also positive for p-ERK (Fig. 7G). The expression pattern held through across samples (Supplementary Figs. S11–S14, each showing consecutive serial sections).

Thus, spatial transcriptomics–derived signatures defined individual epithelial cell populations and correctly predicted protein expression of unique lineage markers.

DISCUSSION

The pancreas and its constitutive acinar cells possess high metabolic activity and undergo rapid cell death under hypoxic conditions (1–4). During this process, granules containing proteolytic and hydrolyzing enzymes are released, resulting in a rapid destruction of cellular components and nucleic acids. As such, a true transcriptomic profile of the physiologically normal pancreas has remained elusive. Due to rapid degradation postmortem, autopsy samples are not suitable for techniques requiring intact RNA, including single-cell RNA sequencing, and are often difficult to examine by immunostaining as well. The mouse pancreas, whereas histologically similar to the human counterpart, does not recapitulate the effects of age and environmental stressors that characterize human life.

As a result, single-cell studies of the human pancreas have included very few samples (74, 75) or embryonic samples (76) and have focused on endocrine cells less susceptible to degradation. Previous autopsy studies on pancreata of patients deceased with no known pancreas pathology revealed frequent PanINs and KRAS mutations (10, 14–17, 31–35, 77; bioRxiv 2023.01.27.525553), but the samples mainly represented older individuals with limited transcriptional profiling performed. In recent years, the advent of single-cell technologies has led to the in-depth characterization of human pancreatic cancer and its accompanying tumor microenvironment (24, 26, 59, 78, 79). In those studies, tumor-specific changes are assessed in comparison with adjacent "normal" pancreas, which is often desmoplastic and inflamed. Thus, the characteristics of the human pancreas, and specifically its complement of non-epithelial cells, have largely remained unexplored.

Figure 6. Spatial transcriptomics reveals a unique epithelial gene signature of PanIN lesions that aligns closely with tumor epithelium. **A,** Left, GeoMX tissue section from a donor pancreas stained for panCK and CD45. panCK$^+$ segments are pseudocolored in green, whereas panCK$^-$CD45$^-$ segments are pseudocolored in red. Right, GeoMX tissue section from surgically resected, treatment-naive PDAC stained for panCK and CD45. panCK$^+$ segments are pseudocolored in purple. **B,** Sankey plot showing the distribution of ROIs in donor or PDAC samples. **C,** Heat map of cell type–specific markers derived from differential gene expression using the linear mixed model on spatial transcriptomic ROIs. **D,** UMAP overlay of disease states on extracted epithelial cells from the single-cell dataset of healthy, adjacent normal, and tumor samples. **E,** AUCell gene set scoring mapped to the epithelial single-cell dataset of healthy, adjacent normal, and tumor samples using signatures derived from acinar, normal duct, PanIN, and ADM spatial transcriptomic ROIs. The top row represents spatial transcriptomic signatures obtained from healthy tissue; the bottom row represents spatial transcriptomic signatures obtained from tumor tissue. **F,** AUCell gene set scoring mapped to the epithelial single-cell dataset of healthy, adjacent normal, and tumor samples using signatures derived from glandular tumor and poorly differentiated tumor ROIs.

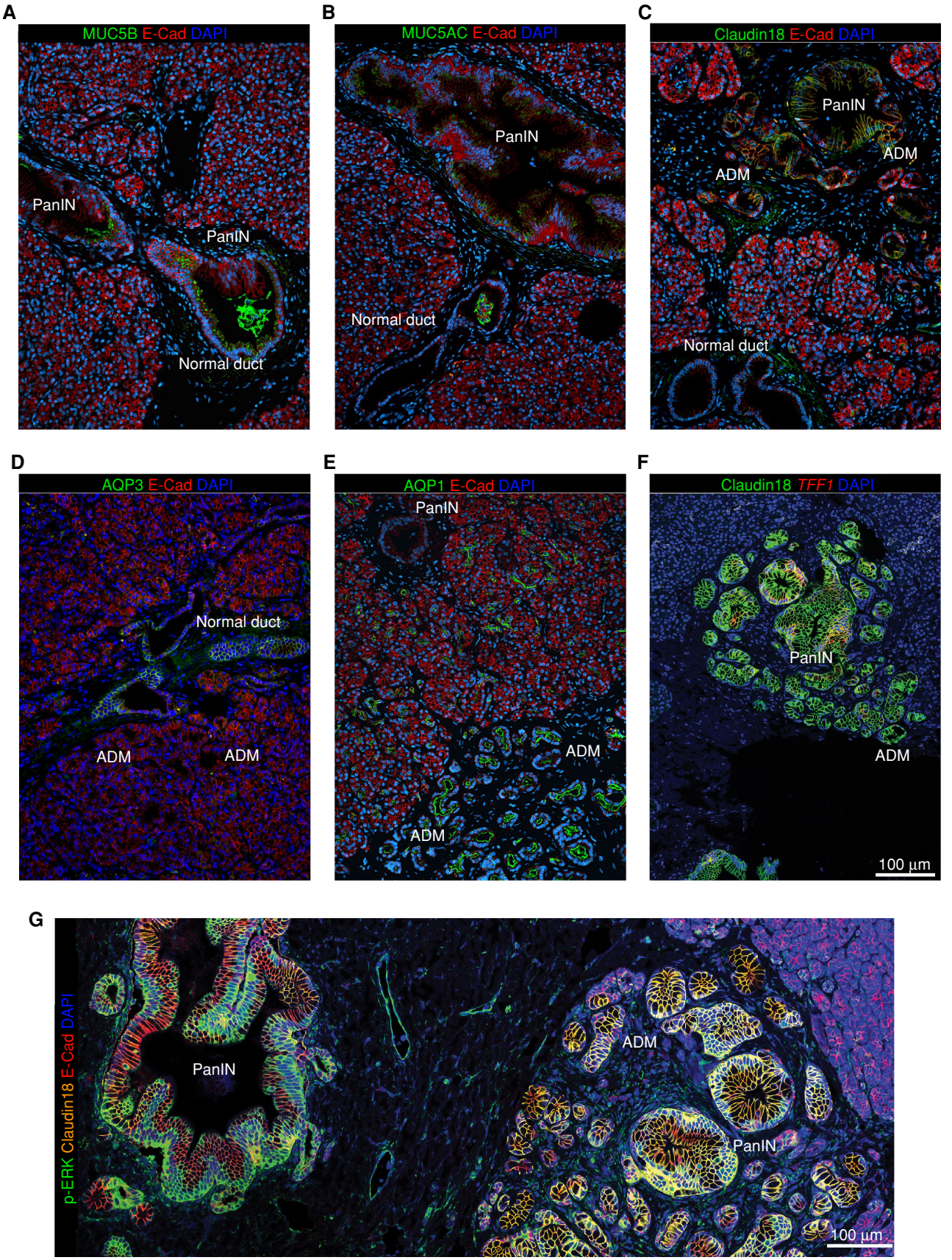
A
MUC5B E-Cad DAPI
PanIN
PanIN
Normal duct
B
MUC5AC E-Cad DAPI
PanIN
Normal duct
C
Claudin18 E-Cad DAPI
PanIN
ADM
ADM
Normal duct
D
AQP3 E-Cad DAPI
Normal duct
ADM
ADM
E
AQP1 E-Cad DAPI
PanIN
ADM
ADM
F
Claudin18 TFF1 DAPI
PanIN
ADM
100 µm
G
p-ERK Claudin18 E-Cad DAPI
PanIN
ADM
PanIN
100 µm

Organ donation provides a unique opportunity to collect human tissue in a controlled manner in which conditions can be optimized to suspend cellular function in a physiologic state, allowing for virtually no warm ischemic time. Histopathology analysis revealed that the majority of our cohort of donor pancreata (slightly over half) presented with PanIN, neoplastic lesions considered progenitors to pancreatic cancer. Although a similar prevalence was observed before, it was in the context of autopsy studies with patients in the seventh and eighth decades of life (14–17, 77). Other investigators have detected a high prevalence of PanINs in the pancreas, but their studies were based on tumor-adjacent normal areas (bioRxiv 2023.01.27.525553). In contrast, our study indicates that PanINs are common in the pancreas of individuals with no known pancreas pathology and occur early in life. Although there was a slight increase in prevalence in the elderly, the broad distribution of ages counters prior beliefs that PanINs accumulate over time. To ensure an accurate assessment of PanIN burden, multiple samples were taken from the head, body, and tail of each donor organ for histologic analysis. We observed no overt difference in prevalence by anatomic region; PanINs, when present, were typically multifocal and widely dispersed throughout the gland. Based on limited sampling, individual PanINs coexpressed multiple *KRAS* mutations, consistent with recent reports (bioRxiv 2023.01.27.525553).

In mice, spontaneous PanIN is virtually never observed; the lack of PanIN in mice might reflect the age difference (mice rarely live to 2 years of age, and most studies are conducted on animals of less than a year old). Further, laboratory mice live in a highly controlled environment with predictable schedules and diets and no risk factors, such as environmental pollution and tobacco use. In addition to PanIN, we observed frequent areas of ADM (dedifferentiation to acinar cells to duct-like cells). In mice, acinar cells are the prevalent source of PanIN, and PanIN is preceded by ADM (80). Duct cells can also give rise to pancreatic cancer, but they appear to do so bypassing the PanIN stage (81, 82). The origin of PanIN and pancreatic cancer is still under debate, and the presence of ADM in human samples has been questioned. Analysis of donor organs showed common ADM and PanIN, but no clear continuality between the two; PanINs were more often contiguous with ducts, consistent with a ductal origin as in previous reports (83–85). However, ADM-associated PanINs were also detected, suggesting that both cell types might serve as the cell of origin (80, 86, 87).

To better understand PanIN lesions in the context of a nondiseased pancreas, we performed a multiparametric analysis of donor pancreatic tissue, pancreatic adenocarcinoma, and adjacent uninvolved tissue. We determined that PanIN lesions and their surrounding microenvironment had a desmoplastic stroma that was vastly different from normal pancreatic acinar tissue, including ADM. PanIN stroma had a unique inflammatory infiltrate that included myeloid cells as well as T helper and cytotoxic T cells. In contrast to tumors, in which Tregs are prevalent (50), few or no Tregs were detected in PanINs. This is also in contrast to murine models (and possibly tumor-associated PanINs) that harbor Tregs adjacent to ADM and PanIN (50). Similar to pancreatic ducts, human PanIN lesions were surrounded by an array of collagen and fibroblasts. Although both expressed FAP, fibroblasts surrounding PanIN lesions also expressed vimentin and SMA—the latter a marker of fibroblast activation. Whether this stroma's main function is to restrain PanIN progression, as shown in experimental models (88, 89), or whether it promotes PanIN progression remains to be determined.

We sought to understand the transcriptional signature of epithelial and stromal cells in the normal pancreas. Our analysis revealed heterogeneous populations of fibroblasts and other mesenchymal cells, such as endothelial cells and pericytes, as well as abundant myeloid cells. As these same cell populations are common in pancreatic cancer stroma, we compared their characteristics between normal pancreata and tumors. Interestingly, nonepithelial cell populations were largely distinct, with gene expression signatures depending on their origin from the normal pancreas or tumors. Differences in gene expression were most notable in fibroblasts, with markers of CAFs, such as the recently described *LRRC15* (90), exclusively expressed in the latter. Of note, our fibroblast populations only partially reflected those described in the healthy mouse pancreas, a finding that might reflect species specificity. In contrast, myeloid cells were less distinct; further analysis revealed that myeloid cells in the normal pancreas displayed a gene signature reminiscent of TAMs. Whether the TAM-like status was present originally or is a by-product of time on life support is unfortunately impossible to determine. Fibroblasts in pancreatic cancer have been described as heterogeneous, with SMA-high, myofibroblast-like myCAFs existing in parallel with iCAFs and antigen-presenting CAFs (23); additional heterogeneity is due to cell of origin and expression of other specific markers (49). Interestingly, in our cohort, fibroblast populations showed a distinct shift in tumors compared with normal pancreas—the latter not clearly reflecting this CAF classification but showing a similar level of heterogeneity.

Lastly, we interrogated the transcriptional signature of PanINs from the healthy pancreas compared with normal acinar and ductal cells, tumor-associated PanINs, and tumor cells. Of note, tissue dissociation during the processing of single-cell RNA sequencing samples makes it impossible to identify PanIN cells within the samples, as spatial and histologic information is lost. To bypass this limitation, we leveraged spatial transcriptomics and then integrated transcriptomic signatures from spatial data with single-cell RNA sequencing data. Interestingly, we observed that PanINs in the normal pancreas and in the tumor transcriptionally have a high degree of concordance, although they also have some distinct features. Additionally, PanINs are transcriptionally

Figure 7. Claudin18, MUC5AC/B, and AQP1/3 distinguish normal ducts, ADM, and PanIN in a healthy pancreas. **A,** Donor tissue stained with antibodies against MUC5B (green) and E-Cadherin (red), along with DAPI. **B,** Donor tissue stained with antibodies against MUC5AC (green) and E-Cadherin (red), along with DAPI. **C,** Donor tissue stained with antibodies against Claudin18 (green) and E-Cadherin (red), along with DAPI. **D,** Donor tissue stained with antibodies against AQP3 (green) and E-Cadherin (red), along with DAPI. **E,** Donor tissue stained with antibodies against AQP1 (green) and E-Cadherin (red), along with DAPI. **F,** Donor tissue stained with RNAScope probe for *TFF1* (red) and antibody against Claudin18 (green), along with DAPI. **G,** Donor tissue stained with antibodies against p-ERK (green), Claudin18 (orange), and E-Cadherin (red), along with DAPI. E-Cad, E-Cadherin.

distinct from ducts and are markedly different from ADM. Surprisingly, the integration of PanIN signatures with our single-cell data revealed that PanINs are transcriptionally closely related to malignant tumors. This finding raises multiple questions; key among those are why PanINs, found frequently in the population, rarely progress to invasive disease given the relatively low incidence of pancreatic cancer. Notably, pancreas transplant patients do not have an increased incidence of pancreatic cancer, indicating that progression remains unlikely even upon induced immunosuppression (91). An intriguing possibility is that the PanIN microenvironment restrains malignant transformation, a direction we plan to pursue in future studies. The endeavor to identify mechanisms that inhibit or promote PanIN progression to malignancy bears important clinical significance, as results may have the possibility to be leveraged for early detection and therapeutic strategies.

METHODS

Donor Sample Procurement

Donor pancreata not eligible for transplant or for whom there were no eligible recipients were collected at the Gift of Life Michigan Donor Care Center. While maintaining blood flow, the superior mesenteric arteries and celiac arteries were cross-clamped and pancreas was recovered and immediately placed in a physiologic organ preservation solution on ice and transported to the University of Michigan, approximately 6 miles away. Acquisition of donor pancreata for research purposes was approved by the Gift of Life research review group. Acquisition of patient tumor samples through formal written or phone consent was described previously (24) and approved by the University of Michigan Institutional Review Board (HUM00025339).

Tissue Processing

Upon arrival to the laboratory, the donor pancreas was dissected by a clinically trained pancreatobiliary surgeon. The organ was dissected into head, body, and tail, with portions of each placed into DMEM with 1% BSA/10 μmol/L Y27632 or 10% formalin for single-cell sequencing or paraffin embedding, respectively. For single-cell processing, tissue was minced into 1-mm^3 pieces and then digested with 1 mg/mL collagenase P for 20 to 30 minutes at 37°C with gentle agitation. Digested tissue was rinsed three times with DMEM/1% BSA/10 μmol/L Y27632 and then filtered through a 40-μm mesh. Resulting cells were submitted to the University of Michigan Advanced Genomics Core for single-cell sequencing using the 10x Genomics Platform.

mfIHC

FFPE tissue slides were rehydrated in triplicate with xylene, followed by a single submersion in 100% ethanol, 95% ethanol, and 70% ethanol, respectively. Rehydrated slides were then washed in neutral buffered formalin and rinsed with deionized water. Antigen retrieval was performed with sodium citrate (pH 6.0) buffer for membrane and cytoplasmic epitopes and tris-EDTA (pH 9.0) buffer for nuclear epitopes. Tissue was blocked using endogenous peroxidase at room temperature, followed by 10% donkey serum overnight at 4°C. Primary antibodies were diluted in 5% donkey serum in TBST and incubated overnight at 4°C. Subsequent multiplex staining was completed using a 1% BSA block. Upon completion of the multiplex, tissue samples were rinsed in deionized water and mounted with DAPI ProLong Diamond Antifade Mountant (Thermo Fisher Scientific). Images were taken using the Vectra Polaris Work Station (Akoya Biosciences). Antibodies/dilutions used are listed in Supplementary Table S5.

Multiplex Immunofluorescence Quantification

Images were acquired using the Mantra Quantitative Pathology Work Station (Akoya Biosciences). A minimum of 10 images were acquired from each tissue section. All cube filters were used for each image capture (DAPI, CY3, CY5, CY7, Texas Red, and Qdot), and the saturation protection feature was utilized. After all images were acquired, they were analyzed using inForm Cell Analysis software (Akoya Biosciences). Using this software, acinar, ductal, ADM, and PanIN samples were batch analyzed by their separate diagnoses, which were confirmed by a pathologist. Cell segmentation was completed using DAPI as a basis of cell location and nuclear size, and all cells were segmented into the following subsets: nucleus, cytoplasm, and membrane. Basic phenotypes were created using the automated training software. For the fibroblast panel, this included vimentin$^+$, SMA$^+$, and PDGFR$^+$. For the immune-based panel, this included CD3$^+$, CD8$^+$, CD163$^+$, PanCK$^+$, and FoxP3$^+$. Software output consisting of mean fluorescent intensity (mfi) of each antibody–fluorophore pair, basic phenotypes, and x and y coordinates was acquired for further processing to determine the relative population of each cell type.

RNAScope Multiplex Fluorescent Detection with Immunofluorescence

RNAScope Multiplex Fluorescent Detection was performed according to instructions provided by the manufacturer [Advanced Cell Diagnostics (ACD)]. Briefly, 5-μm thick FFPE normal pancreas tissue sections were mounted on charged slides and baked at 60°C for 1 hour, deparaffinized, dehydrated, and washed with 0.1% Tween-20 RNAse-free 1× phosphate-buffered saline (PBST) three times. This was followed by incubation with hydrogen peroxide for 10 minutes at room temperature and target retrieval for 15 minutes at 98°C. Slides were then blocked with codetection antibody diluent (ACD) for 30 minutes prior to incubation with Claudin18 primary antibody (1:100 in codetection antibody diluent) for 24 hours at 4°C. The next day, the tissue sections were fixed with formalin and treated with ProteasePlus Reagent (ACD) for 13 minutes at 40°C. Amplification and signal enhancement (AMP) were performed for two different probes/channels (C1 and C2). The TFF1-C1 probe was at 1× concentration, whereas the CCL2-C2 probe was at 50× concentration. The probes were diluted as per the manufacturer's instructions, and slides were incubated with them at 40°C for 2 hours. Then the slides were washed with RNA scope washing buffer (ACD) twice. Signal for each of the probes was amplified with AMP reagents, horseradish peroxidase, and the tyramide signal amplification (TSA) kit (ACD) at 40°C. Slides were then washed with PBST three times and incubated with anti-rabbit secondary Alexa Fluor IgG (H + L) antibody (1:400 in codetection antibody diluent) for 1 hour at room temperature. Finally, slides were incubated with DAPI for 15 minutes and washed three times with PBST prior to being mounted with ProLong Diamond Antifade. Antibodies and RNAScope probes are listed in Supplementary Table S6.

Immunofluorescence Assessment with Tyramide Signal Amplification

FFPE normal pancreas tissue sections (5-μm thick) were mounted on charged slides and baked at 60°C for 1 hour, deparaffinized, and dehydrated. Slides were then washed with deionized water for 2 minutes followed by antigen retrieval at 96°C with 10 mmol/L sodium citrate (pH 6.0) for 8 min. Once the slides cooled to room temperature, they were washed three times (2 minutes per wash) with PBS and endogenous peroxides were quenched with 3% hydrogen peroxide for 15 minutes. The TSA kit (Invitrogen) was used according to the manufacturer's instructions. Briefly, slides were incubated with blocking serum provided in the kit and stained with antigen-specific primary antibodies overnight at 4°C: Claudin18 (1:100), AQP1 (1:500), AQP3 (1:200), MUC5AC (1:200), or MUC5B (1:200). The next day, slides

were washed three times with PBS and incubated in anti-rabbit secondary antibody for 1 hour. This was followed by an additional three washes with PBS. TSA conjugated to 488 or 555 fluorophores was applied for 10 minutes, followed by incubation with a reaction stop solution for 5 minutes. Finally, slides were incubated with DAPI for 5 minutes and washed three times with PBS prior to being mounted with ProLong Diamond Antifade. High-magnification images were obtained using confocal microscopy (Leica Stellaris 8). Antibodies used are listed in Supplementary Table S5.

Single-Cell RNA Sequencing

Samples were run using 50-cycle paired-end reads on the NovaSeq 6000 (Illumina) to a depth of 100,000 reads. Cell Ranger count version 6.0 was used with default settings, with an initially expected cell count of 10,000. The GRCh38 reference genome was used for alignment. Ambient RNA correction was done for each sample independently using SoupX (92). Briefly, SoupX estimates the ambient RNA profile from the cell-free RNA and then estimates the cell-specific contamination fraction using a set of user-specified negative markers. Then, we used Seurat's (93) recommended workflow for single-cell RNA sequencing data processing and integration. Briefly, we removed low-quality cells with more than a 15% fraction of mitochondrial gene expression or less than 200 features (genes) detected. Expression was then log-normalized to the library size, and the top 2,000 highly variable features were extracted and scaled for downstream analysis. For sample integration, we used reciprocal PCA (rPCA), as it is preferred for datasets with several mutually exclusive cell populations and it scales better with a larger number of samples. Count matrices were integrated to account for batch effects. Using the integrated feature matrix, we ran PCA to collapse gene expression to fewer principal components (35 principal components), and then Louvain clustering was done to define different cell clusters. We used UMAP dimension reduction to create two-dimensional embedding for the cells. For cell-type annotation, we used a panel of previously known markers for different cell types in pancreatic tissue to define different cell populations. Differential cell–cell communication was performed using CellChat (94). Briefly, cell–cell communication was calculated between each cell-type pair using the manually curated interaction database (CellChatDB) separately on tumor and healthy donor samples. Then, differential cell–cell communication weight of tumor versus healthy was calculated for each cell-type pair.

Pseudobulk RNA Differential Gene Expression

We aggregated the counts from different samples for all (or a subset of) cells. We used DESeq2 for normalization and differential gene expression (DGE) analysis of the samples. We used PCAtools (https://www.bioconductor.org/packages/release/bioc/html/PCAtools.html) to perform and visualize PCA on the samples and Pearson correlation to determine the correlation between the samples. Gene Ontology analysis was done using the ClusterProfiler (95) package on the upregulated genes.

Differential Abundance

We used miloR to define differentially abundant cell populations (44). MiloR defines neighborhoods of cells using KNN graphs; after that, it uses negative-binomial regression to determine neighborhoods with differential abundance in one condition compared with the other. We set the K parameter for constructing the KNN graph to 60, as it yielded neighborhoods with a mean of 150 cells, which is roughly equal 3 times the number of samples as recommended by miloR authors.

Gene Set Scoring

For scoring different gene sets, we used the AUCell (96) package. AUCell gives a score of a specific gene set for each cell using its raw counts, which makes it invariant to any downstream normalization or integration. Acinar, ductal, and tumor cell gene signatures were utilized from the literature (59). We used the Molecular Signatures Database (MSigDB; ref. 97) Hallmark gene sets for KRAS activity score.

Spatial Transcriptomics Data Analysis

We used the GeoMxWorkflows package (https://bioconductor.org/packages/release/workflows/html/GeoMxWorkflows.html) for quality control and processing of NanoString GeoMx data. Briefly, quality control was performed to exclude the ROIs with less than 10% gene detection rate (less than 10% of the original Whole Transcriptome Atlas (WTA) panel genes were detected) and exclude genes detected in less than 10% of the ROIs. Q3 normalization was performed for each ROI in the gene expression matrix followed by log normalization. For visualization purposes, we performed PCA, which clearly showed a batch effect. We used limma package (98) batch correction function to regress out the batch effect, which showed the clustering of ROIs from the same cell type together. To define cell type–specific markers, we used a linear mixed model to perform DGE between each cell type and the rest of the ROIs, similar to how we define markers in single-cell data. The top 20 significantly upregulated marker genes were then used as a gene set for scoring using AUCell (96). The scores were then scaled and visualized on the UMAPs of the acinar/ductal cell subset. To score different PDAC subtypes (classic, basal, exocrine-like, and ADEX) for each ROI, we used GSVA (99).

gDNA Isolation from the Preneoplastic Lesion

Ten slides of 5-μm thickness were sectioned from two FFPE tissue blocks (AIFR291_C1, AII1271_C1). One slide from both cases was stained with hematoxylin and eosin (H&E) and reviewed by a pathologist to identify the location of the preneoplastic lesion for macrodissection on the remaining nine slides. gDNA for each sample was extracted using Qiagen's QIAamp DNA FFPE Tissue Kit (Qiagen, cat. #56404).

Detection of KRAS Mutations by Digital Droplet PCR (06745_T)

Assays specific for the detection of G12D, G12R, and G12V in KRAS were ordered through Bio-Rad (assay IDs: G12D-dHsaCP2000001, G12R-dHsaMDS615795490, G12V-dHsaCP2000005). Cycling conditions were tested to ensure optimal annealing/extension temperature, as well as optimal separation of positive from empty droplets. Optimization was done with a known positive control.

After PicoGreen quantification, 9 ng gDNA was combined with locus-specific primers, FAM- and HEX-labeled probes, MseI, and digital PCR Supermix for probes (no dUTP). All reactions were performed on a QX200 ddPCR system (Bio-Rad, cat. #1864001) and each sample was evaluated in technical triplicates. Reactions were partitioned into an average of ~20,000 droplets per well using the QX200 droplet generator. Emulsified PCRs were run on a 96-well thermal cycler using cycling conditions identified during the optimization step (95°C 10 minutes; 40 cycles of 94°C 30 minutes and 55°C 1 minute; 98°C 10 minutes; 4°C hold). Plates were read and analyzed with the QuantaSoft software to assess the number of droplets positive for mutant DNA, wild-type DNA, both, or neither.

Data Availability

Raw human data from the Steele and colleagues' study (24) are available at the NIH database of Genotypes and Phenotypes (dbGaP) under the accession phs002071.v1.p1. Raw single-cell sequencing data from donor pancreata are available at the NIH dbGaP database under the accession phs003229. NanoString GeoMX data are available from the NIH Gene Expression Omnibus database under the accession number GSE226829 (https://www.ncbi.nlm.nih.gov/geo/query/acc.cgi?acc=GSE226829) and feature matrices of single-cell RNA data are available at accession number GSE229413 (https://www.ncbi.nlm.nih.gov/geo/query/acc.cgi?acc=GSE229413). Whole slide scans of H&E sections from the head (i), body (ii), and tail (iii) of all donor pancreata, taken at 1:4 magnification, are available at the Zenodo image repository at https://doi.org/10.5281/zenodo.7683038.

Code Availability

All codes used for this study are publicly available at the following GitHub: https://github.com/PascaDiMagliano-Lab/GoL_public_repo.

Authors' Disclosures

V. Sahai reports grants from Actuate Therapeutics, Bristol Myers Squibb, Celgene, Clovis, MedImmune, the NCI, Relay, Repare, Syros, Exelixis, and Fibrogen, grants, personal fees, and nonfinancial support from Cornerstone, grants and personal fees from Agios/Servier, Incyte, and Ipsen, personal fees from AstraZeneca, Autem, Delcath, GSK, Helsinn, Histosonics, Kinnate, Lynx/Amplity, and Taiho, and nonfinancial support from BeiGene, the American Society of Clinical Oncology, and the Cholangiocarcinoma Foundation outside the submitted work. A. Rao reports grants from the NIH and the American Cancer Society, and other support from University of Michigan, Ann Arbor, during the conduct of the study; other support from Agilent Technologies and Voxel Analytics, LLC, grants from the NIH, the National Science Foundation, and the Department of Defense, and grants and other support from Astellas Pharma and University of Michigan, Ann Arbor, outside the submitted work. J. Shi reports grants from the NCI during the conduct of the study, as well as grants from the NCI outside the submitted work. T.L. Frankel reports grants from the NIH and the Veterans Administration during the conduct of the study. No disclosures were reported by the other authors.

Disclaimer

The funders had no role in study design, data collection and analysis, decision to publish, or preparation of the manuscript.

Authors' Contributions

E.S. Carpenter: Conceptualization, data curation, formal analysis, supervision, validation, investigation, visualization, methodology, writing–original draft, writing–review and editing. **A.M. Elhossiny:** Conceptualization, data curation, formal analysis, validation, investigation, visualization, methodology, writing–original draft, writing–review and editing. **P. Kadiyala:** Conceptualization, data curation, formal analysis, validation, investigation, visualization, methodology, writing–review and editing. **J. Li:** Conceptualization, data curation, formal analysis, validation, investigation, visualization, methodology, writing–review and editing. **J. McGue:** Data curation, formal analysis, validation, investigation, visualization, methodology, writing–review and editing. **B.D. Griffith:** Data curation, formal analysis, investigation, methodology, writing–review and editing. **Y. Zhang:** Data curation, formal analysis, validation, investigation, visualization, methodology, writing–review and editing. **J. Edwards:** Data curation, formal analysis, methodology. **S. Nelson:** Data curation, formal analysis, investigation, methodology. **F. Lima:** Data curation, formal analysis. **K.L. Donahue:** Data curation. **W. Du:** Data curation. **A.C. Bischoff:** Formal analysis, methodology. **D. Alomari:** Data curation. **H.R. Watkoske:** Data curation. **M. Mattea:** Resources. **S. The:** Methodology. **C.E. Espinoza:** Resources. **M. Barrett:** Resources. **C.J. Sonnenday:** Conceptualization, resources. **N. Olden:** Resources, data curation. **C.-T. Chen:** Data curation, investigation, methodology. **N. Peterson:** Data curation. **V. Gunchick:** Data curation, methodology. **V. Sahai:** Data curation, methodology. **A. Rao:** Conceptualization, formal analysis, supervision, investigation, methodology, project administration, writing–review and editing. **F. Bednar:** Conceptualization, data curation, formal analysis, supervision, investigation, visualization, writing–original draft, writing–review and editing. **J. Shi:** Data curation, visualization, writing–review and editing. **T.L. Frankel:** Conceptualization, resources, supervision, funding acquisition, investigation, methodology, writing–original draft, project administration, writing–review and editing. **M. Pasca di Magliano:** Conceptualization, resources, supervision, funding acquisition, investigation, methodology, writing–original draft, project administration, writing–review and editing.

Acknowledgments

We sincerely thank Gift of Life Michigan and donors and their families who have generously provided organs for this research. We thank T. Tamsen, M. Hogan, and J. Opp from the University of Michigan Advanced Genomics Core for their assistance with single-cell RNA sequencing and spatial transcriptomics. We acknowledge the use of the Integrated Genomics Operation Core at the Memorial Sloan Kettering Cancer Center, funded by an NCI Cancer Center Support Grant (CCSG; P30 CA08748), Cycle for Survival, and the Marie-Josée and Henry R. Kravis Center for Molecular Oncology. This work was supported by R01-CA268426 to M. Pasca di Magliano and T.L. Frankel. Work in the M. Pasca di Magliano laboratory was also supported by NIH/NCI grants R01-CA260752, R01-CA271510, U01-CA224145, U01-CA274154, and U54CA274371. Work in the T.L. Frankel laboratory was supported by NIH/NCI grant U01CA274154, NIH/National Institute of Diabetes and Digestive and Kidney Diseases (NIDDK) 5R01DK128102, and VA BLR&D Merit Award 5I01BX005777. E.S. Carpenter was supported by the VA BLR&D CDA IK2BX005875, the American College of Gastroenterology CDA, and by NIH/NIDDK T32-DK094775. A.M. Elhossiny was supported by the Rackham International Student Fellowship. P. Kadiyala was supported by NIH/National Institute of Allergy and Infectious Diseases T32-AI007413 and NIH/National Institute of General Medical Sciences (NIGMS) T32-GM113900. J. Li was supported by NIH/NIGMS T32GM007863. K.L. Donahue was supported by NIH/NCI F31-CA265085-01A1. A. Rao was supported by NCI grants R37-CA214955 and CCSG Bioinformatics Shared Resource 5 P30 CA046592. F. Bednar was funded by the Association for Academic Surgery Joel J. Roslyn Award and NCI R01-CA271510. J. Shi was funded by NIH/NCI K08CA234222 and R37CA262209.

The publication costs of this article were defrayed in part by the payment of publication fees. Therefore, and solely to indicate this fact, this article is hereby marked "advertisement" in accordance with 18 USC section 1734.

Note

Supplementary data for this article are available at Cancer Discovery Online (http://cancerdiscovery.aacrjournals.org/).

Received January 13, 2023; revised March 3, 2023; accepted March 15, 2023; published first April 6, 2023.

REFERENCES

1. Walker AE. The adult pancreas in trauma and disease. Acad Forensic Pathol 2018;8:192–218.
2. Morioka F, Tani N, Ikeda T, Hirokawa T, Ikeda K, Shida A, et al. Morphological and biochemical changes in the pancreas associated with acute systemic hypoxia. Hum Cell 2021;34:400–18.
3. Cocariu EA, Mageriu V, Staniceanu F, Bastian A, Socoliuc C, Zurac S. Correlations between the autolytic changes and postmortem interval in refrigerated cadavers. Rom J Intern Med 2016;54:105–12.
4. Shimizu M, Hayashi T, Saitoh Y, Ohta K, Itoh H. Postmortem autolysis in the pancreas: multivariate statistical study: the influence of clinicopathological conditions. Pancreas 1990;5:91–4.
5. Grant TJ, Hua K, Singh A. Molecular pathogenesis of pancreatic cancer. Prog Mol Biol Transl Sci 2016;144:241–75.
6. Luchini C, Grillo F, Fassan M, Vanoli A, Capelli P, Paolino G, et al. Malignant epithelial/exocrine tumors of the pancreas. Pathologica 2020;112:210–26.
7. Matthaei H, Schulick RD, Hruban RH, Maitra A. Cystic precursors to invasive pancreatic cancer. Nat Rev Gastroenterol Hepatol 2011;8:141–50.
8. Zamboni G, Hirabayashi K, Castelli P, Lennon AM. Precancerous lesions of the pancreas. Best Pract Res Clin Gastroenterol 2013;27:299–322.
9. Assarzadegan N, Babaniamansour S, Shi J. Updates in the diagnosis of intraductal neoplasms of the pancreas. Front Physiol 2022;13:856803.

10. Hruban RH, Takaori K, Klimstra DS, Adsay NV, Albores-Saavedra J, Biankin AV, et al. An illustrated consensus on the classification of pancreatic intraepithelial neoplasia and intraductal papillary mucinous neoplasms. Am J Surg Pathol 2004;28:977–87.
11. Biankin AV, Kench JG, Biankin SA, Lee CS, Morey AL, Dijkman FP, et al. Pancreatic intraepithelial neoplasia in association with intraductal papillary mucinous neoplasms of the pancreas: implications for disease progression and recurrence. Am J Surg Pathol 2004;28:1184–92.
12. Konstantinidis IT, Vinuela EF, Tang LH, Klimstra DS, D'Angelica MI, Dematteo RP, et al. Incidentally discovered pancreatic intraepithelial neoplasia: what is its clinical significance? Ann Surg Oncol 2013;20:3643–7.
13. Yu DY, Yu YD, Kim WB, Han HJ, Choi SB, Kim DS, et al. Clinical significance of pancreatic intraepithelial neoplasia in resectable pancreatic cancer on survivals. Ann Surg Treat Res 2018;94:247–53.
14. Matsuda Y, Furukawa T, Yachida S, Nishimura M, Seki A, Nonaka K, et al. The prevalence and clinicopathological characteristics of high-grade pancreatic intraepithelial neoplasia: autopsy study evaluating the entire pancreatic parenchyma. Pancreas 2017;46:658–64.
15. Longnecker DS, Suriawinata AA. Incidence of pancreatic intraepithelial neoplasia in an autopsy series. Pancreas 2022;51:305–9.
16. Schwartz AM, Henson DE. Familial and sporadic pancreatic carcinoma, epidemiologic concordance. Am J Surg Pathol 2007;31:645–6.
17. Andea A, Sarkar F, Adsay VN. Clinicopathological correlates of pancreatic intraepithelial neoplasia: a comparative analysis of 82 cases with and 152 cases without pancreatic ductal adenocarcinoma. Mod Pathol 2003;16:996–1006.
18. Cubilla AL, Fitzgerald PJ. Morphological lesions associated with human primary invasive nonendocrine pancreas cancer. Cancer Res 1976;36:2690–8.
19. Waddell N, Pajic M, Patch AM, Chang DK, Kassahn KS, Bailey P, et al. Whole genomes redefine the mutational landscape of pancreatic cancer. Nature 2015;518:495–501.
20. Biankin AV, Waddell N, Kassahn KS, Gingras MC, Muthuswamy LB, Johns AL, et al. Pancreatic cancer genomes reveal aberrations in axon guidance pathway genes. Nature 2012;491:399–405.
21. Jones S, Zhang X, Parsons DW, Lin JC, Leary RJ, Angenendt P, et al. Core signaling pathways in human pancreatic cancers revealed by global genomic analyses. Science 2008;321:1801–6.
22. Yachida S, Jones S, Bozic I, Antal T, Leary R, Fu B, et al. Distant metastasis occurs late during the genetic evolution of pancreatic cancer. Nature 2010;467:1114–7.
23. Elyada E, Bolisetty M, Laise P, Flynn WF, Courtois ET, Burkhart RA, et al. Cross-species single-cell analysis of pancreatic ductal adenocarcinoma reveals antigen-presenting cancer-associated fibroblasts. Cancer Discov 2019;9:1102–23.
24. Steele NG, Carpenter ES, Kemp SB, Sirihorachai V, The S, Delrosario L, et al. Multimodal mapping of the tumor and peripheral blood immune landscape in human pancreatic cancer. Nat Cancer 2020;1:1097–112.
25. Peng J, Sun BF, Chen CY, Zhou JY, Chen YS, Chen H, et al. Single-cell RNA-seq highlights intra-tumoral heterogeneity and malignant progression in pancreatic ductal adenocarcinoma. Cell Res 2019;29:725–38.
26. Raghavan S, Winter PS, Navia AW, Williams HL, DenAdel A, Lowder KE, et al. Microenvironment drives cell state, plasticity, and drug response in pancreatic cancer. Cell 2021;184:6119–37.
27. Balachandran VP, Luksza M, Zhao JN, Makarov V, Moral JA, Remark R, et al. Identification of unique neoantigen qualities in long-term survivors of pancreatic cancer. Nature 2017;551:512–6.
28. Carstens JL, Correa de Sampaio P, Yang D, Barua S, Wang H, Rao A, et al. Spatial computation of intratumoral T cells correlates with survival of patients with pancreatic cancer. Nat Commun 2017;8:15095.
29. Tsujikawa T, Kumar S, Borkar RN, Azimi V, Thibault G, Chang YH, et al. Quantitative multiplex immunohistochemistry reveals myeloid-inflamed tumor-immune complexity associated with poor prognosis. Cell Rep 2017;19:203–17.
30. Clark CE, Hingorani SR, Mick R, Combs C, Tuveson DA, Vonderheide RH. Dynamics of the immune reaction to pancreatic cancer from inception to invasion. Cancer Res 2007;67:9518–27.
31. Feldmann G, Beaty R, Hruban RH, Maitra A. Molecular genetics of pancreatic intraepithelial neoplasia. J Hepatobiliary Pancreat Surg 2007;14:224–32.
32. Yanagisawa A, Ohtake K, Ohashi K, Hori M, Kitagawa T, Sugano H, et al. Frequent c-Ki-ras oncogene activation in mucous cell hyperplasias of pancreas suffering from chronic inflammation. Cancer Res 1993;53:953–6.
33. Terhune PG, Phifer DM, Tosteson TD, Longnecker DS. K-ras mutation in focal proliferative lesions of human pancreas. Cancer Epidemiol Biomarkers Prev 1998;7:515–21.
34. Heinmoller E, Dietmaier W, Zirngibl H, Heinmoller P, Scaringe W, Jauch KW, et al. Molecular analysis of microdissected tumors and preneoplastic intraductal lesions in pancreatic carcinoma. Am J Pathol 2000;157:83–92.
35. Wilentz RE, Iacobuzio-Donahue CA, Argani P, McCarthy DM, Parsons JL, Yeo CJ, et al. Loss of expression of Dpc4 in pancreatic intraepithelial neoplasia: evidence that DPC4 inactivation occurs late in neoplastic progression. Cancer Res 2000;60:2002–6.
36. Collins MA, Yan W, Sebolt-Leopold JS, Pasca di Magliano M. MAPK signaling is required for dedifferentiation of acinar cells and development of pancreatic intraepithelial neoplasia in mice. Gastroenterology 2014;146:822–34.
37. Hingorani SR, Petricoin EF, Maitra A, Rajapakse V, King C, Jacobetz MA, et al. Preinvasive and invasive ductal pancreatic cancer and its early detection in the mouse. Cancer Cell 2003;4:437–50.
38. Hingorani SR, Wang L, Multani AS, Combs C, Deramaudt TB, Hruban RH, et al. Trp53R172H and KrasG12D cooperate to promote chromosomal instability and widely metastatic pancreatic ductal adenocarcinoma in mice. Cancer Cell 2005;7:469–83.
39. Collins MA, Bednar F, Zhang Y, Brisset JC, Galban S, Galban CJ, et al. Oncogenic Kras is required for both the initiation and maintenance of pancreatic cancer in mice. J Clin Invest 2012;122:639–53.
40. Buechler MB, Pradhan RN, Krishnamurty AT, Cox C, Calviello AK, Wang AW, et al. Cross-tissue organization of the fibroblast lineage. Nature 2021;593:575–9.
41. Dominguez CX, Muller S, Keerthivasan S, Koeppen H, Hung J, Gierke S, et al. Single-cell RNA sequencing reveals stromal evolution into LRRC15(+) myofibroblasts as a determinant of patient response to cancer immunotherapy. Cancer Discov 2020;10:232–53.
42. Helms EJ, Berry MW, Chaw RC, DuFort CC, Sun D, Onate MK, et al. Mesenchymal lineage heterogeneity underlies nonredundant functions of pancreatic cancer-associated fibroblasts. Cancer Discov 2022;12:484–501.
43. Hosein AN, Huang H, Wang Z, Parmar K, Du W, Huang J, et al. Cellular heterogeneity during mouse pancreatic ductal adenocarcinoma progression at single-cell resolution. JCI Insight 2019;5:e129212.
44. Dann E, Henderson NC, Teichmann SA, Morgan MD, Marioni JC. Differential abundance testing on single-cell data using k-nearest neighbor graphs. Nat Biotechnol 2022;40:245–53.
45. Ramilowski JA, Goldberg T, Harshbarger J, Kloppmann E, Lizio M, Satagopam VP, et al. A draft network of ligand-receptor-mediated multicellular signalling in human. Nat Commun 2015;6:7866.
46. Ardito CM, Gruner BM, Takeuchi KK, Lubeseder-Martellato C, Teichmann N, Mazur PK, et al. EGF receptor is required for KRAS-induced pancreatic tumorigenesis. Cancer Cell 2012;22:304–17.
47. Navas C, Hernandez-Porras I, Schuhmacher AJ, Sibilia M, Guerra C, Barbacid M. EGF receptor signaling is essential for k-ras oncogene-driven pancreatic ductal adenocarcinoma. Cancer Cell 2012;22:318–30.
48. Djurec M, Grana O, Lee A, Troule K, Espinet E, Cabras L, et al. Saa3 is a key mediator of the protumorigenic properties of cancer-associated fibroblasts in pancreatic tumors. Proc Natl Acad Sci U S A 2018;115:E1147–E56.
49. Hingorani SR. Epithelial and stromal co-evolution and complicity in pancreatic cancer. Nat Rev Cancer 2023;23:57–77.
50. Zhang Y, Lazarus J, Steele NG, Yan W, Lee HJ, Nwosu ZC, et al. Regulatory T-cell depletion alters the tumor microenvironment and accelerates pancreatic carcinogenesis. Cancer Discov 2020;10:422–39.
51. Nywening TM, Belt BA, Cullinan DR, Panni RZ, Han BJ, Sanford DE, et al. Targeting both tumour-associated CXCR2(+) neutrophils and CCR2(+) macrophages disrupts myeloid recruitment and improves chemotherapeutic responses in pancreatic ductal adenocarcinoma. Gut 2018;67:1112–23.

52. DeNardo DG, Ruffell B. Macrophages as regulators of tumour immunity and immunotherapy. Nat Rev Immunol 2019;19:369–82.
53. Kemp SB, Steele NG, Carpenter ES, Donahue KL, Bushnell GG, Morris AH, et al. Pancreatic cancer is marked by complement-high blood monocytes and tumor-associated macrophages. Life Sci Alliance 2021;4:e202000935.
54. Kemp SB, Carpenter ES, Steele NG, Donahue KL, Nwosu ZC, Pacheco A, et al. Apolipoprotein E promotes immune suppression in pancreatic cancer through NF-kappaB-mediated production of CXCL1. Cancer Res 2021;81:4305–18.
55. Yang X, Lin Y, Shi Y, Li B, Liu W, Yin W, et al. FAP promotes immunosuppression by cancer-associated fibroblasts in the tumor microenvironment via STAT3-CCL2 signaling. Cancer Res 2016;76:4124–35.
56. Sivakumar S, Abu-Shah E, Ahern DJ, Arbe-Barnes EH, Jainarayanan AK, Mangal N, et al. Activated regulatory T-cells, dysfunctional and senescent T-cells hinder the immunity in pancreatic cancer. Cancers (Basel) 2021;13:1776.
57. Bresnick AR, Weber DJ, Zimmer DB. S100 proteins in cancer. Nat Rev Cancer 2015;15:96–109.
58. Simeonov KP, Byrns CN, Clark ML, Norgard RJ, Martin B, Stanger BZ, et al. Single-cell lineage tracing of metastatic cancer reveals selection of hybrid EMT states. Cancer Cell 2021;39:1150–62.
59. Cui Zhou D, Jayasinghe RG, Chen S, Herndon JM, Iglesia MD, Navale P, et al. Spatially restricted drivers and transitional cell populations cooperate with the microenvironment in untreated and chemo-resistant pancreatic cancer. Nat Genet 2022;54:1390–405.
60. Liberzon A, Birger C, Thorvaldsdottir H, Ghandi M, Mesirov JP, Tamayo P. The Molecular Signatures Database (MSigDB) hallmark gene set collection. Cell Syst 2015;1:417–25.
61. Arsenijevic T, Perret J, Van Laethem JL, Delporte C. Aquaporins involvement in pancreas physiology and in pancreatic diseases. Int J Mol Sci 2019;20:5052.
62. Balague C, Gambus G, Carrato C, Porchet N, Aubert JP, Kim YS, et al. Altered expression of MUC2, MUC4, and MUC5 mucin genes in pancreas tissues and cancer cell lines. Gastroenterology 1994;106:1054–61.
63. Tanaka M, Shibahara J, Fukushima N, Shinozaki A, Umeda M, Ishikawa S, et al. Claudin-18 is an early-stage marker of pancreatic carcinogenesis. J Histochem Cytochem 2011;59:942–52.
64. Arumugam T, Brandt W, Ramachandran V, Moore TT, Wang H, May FE, et al. Trefoil factor 1 stimulates both pancreatic cancer and stellate cells and increases metastasis. Pancreas 2011;40:815–22.
65. Guppy NJ, El-Bahrawy ME, Kocher HM, Fritsch K, Qureshi YA, Poulsom R, et al. Trefoil factor family peptides in normal and diseased human pancreas. Pancreas 2012;41:888–96.
66. Kim GE, Bae HI, Park HU, Kuan SF, Crawley SC, Ho JJ, et al. Aberrant expression of MUC5AC and MUC6 gastric mucins and sialyl Tn antigen in intraepithelial neoplasms of the pancreas. Gastroenterology 2002;123:1052–60.
67. Beinrohr L, Murray-Rust TA, Dyksterhuis L, Zavodszky P, Gal P, Pike RN, et al. Serpins and the complement system. Methods Enzymol 2011;499:55–75.
68. Suzuki R, Okubo Y, Takagi T, Sugimoto M, Sato Y, Irie H, et al. The complement C3a-C3a receptor axis regulates epithelial-to-mesenchymal transition by activating the ERK pathway in pancreatic ductal adenocarcinoma. Anticancer Res 2022;42:1207–15.
69. Moffitt RA, Marayati R, Flate EL, Volmar KE, Loeza SG, Hoadley KA, et al. Virtual microdissection identifies distinct tumor- and stroma-specific subtypes of pancreatic ductal adenocarcinoma. Nat Genet 2015;47:1168–78.
70. Bailey P, Chang DK, Nones K, Johns AL, Patch AM, Gingras MC, et al. Genomic analyses identify molecular subtypes of pancreatic cancer. Nature 2016;531:47–52.
71. Collisson EA, Sadanandam A, Olson P, Gibb WJ, Truitt M, Gu S, et al. Subtypes of pancreatic ductal adenocarcinoma and their differing responses to therapy. Nat Med 2011;17:500–3.
72. Juiz N, Elkaoutari A, Bigonnet M, Gayet O, Roques J, Nicolle R, et al. Basal-like and classical cells coexist in pancreatic cancer revealed by single-cell analysis on biopsy-derived pancreatic cancer organoids from the classical subtype. FASEB J 2020;34:12214–28.
73. Kanda M, Matthaei H, Wu J, Hong SM, Yu J, Borges M, et al. Presence of somatic mutations in most early-stage pancreatic intraepithelial neoplasia. Gastroenterology 2012;142:730–3.
74. Tabula Sapiens C, Jones RC, Karkanias J, Krasnow MA, Pisco AO, Quake SR, et al. The Tabula Sapiens: a multiple-organ, single-cell transcriptomic atlas of humans. Science 2022;376:eabl4896.
75. Enge M, Arda HE, Mignardi M, Beausang J, Bottino R, Kim SK, et al. Single-cell analysis of human pancreas reveals transcriptional signatures of aging and somatic mutation patterns. Cell 2017;171:321–30.
76. Olaniru OE, Kadolsky U, Kannambath S, Vaikkinen H, Fung K, Dhami P, et al. Single-cell transcriptomic and spatial landscapes of the developing human pancreas. Cell Metab 2023;35:184–99.
77. Lohr M, Kloppel G, Maisonneuve P, Lowenfels AB, Luttges J. Frequency of K-ras mutations in pancreatic intraductal neoplasias associated with pancreatic ductal adenocarcinoma and chronic pancreatitis: a meta-analysis. Neoplasia 2005;7:17–23.
78. Bernard V, Semaan A, Huang J, San Lucas FA, Mulu FC, Stephens BM, et al. Single-cell transcriptomics of pancreatic cancer precursors demonstrates epithelial and microenvironmental heterogeneity as an early event in neoplastic progression. Clin Cancer Res 2019;25:2194–205.
79. Freed-Pastor WA, Lambert LJ, Ely ZA, Pattada NB, Bhutkar A, Eng G, et al. The CD155/TIGIT axis promotes and maintains immune evasion in neoantigen-expressing pancreatic cancer. Cancer Cell 2021;39:1342–60.
80. Kopp JL, von Figura G, Mayes E, Liu FF, Dubois CL, Morris JP, et al. Identification of Sox9-dependent acinar-to-ductal reprogramming as the principal mechanism for initiation of pancreatic ductal adenocarcinoma. Cancer Cell 2012;22:737–50.
81. Kopp JL, Dubois CL, Schaeffer DF, Samani A, Taghizadeh F, Cowan RW, et al. Loss of pten and activation of kras synergistically induce formation of intraductal papillary mucinous neoplasia from pancreatic ductal cells in mice. Gastroenterology 2018;154:1509–23.
82. Bailey JM, Hendley AM, Lafaro KJ, Pruski MA, Jones NC, Alsina J, et al. p53 mutations cooperate with oncogenic Kras to promote adenocarcinoma from pancreatic ductal cells. Oncogene 2016;35:4282–8.
83. Strobel O, Rosow DE, Rakhlin EY, Lauwers GY, Trainor AG, Alsina J, et al. Pancreatic duct glands are distinct ductal compartments that react to chronic injury and mediate Shh-induced metaplasia. Gastroenterology 2010;138:1166–77.
84. Hruban RH, Adsay NV, Albores-Saavedra J, Compton C, Garrett ES, Goodman SN, et al. Pancreatic intraepithelial neoplasia: a new nomenclature and classification system for pancreatic duct lesions. Am J Surg Pathol 2001;25:579–86.
85. Hruban RH, Goggins M, Parsons J, Kern SE. Progression model for pancreatic cancer. Clin Cancer Res 2000;6:2969–72.
86. Lee AYL, Dubois CL, Sarai K, Zarei S, Schaeffer DF, Sander M, et al. Cell of origin affects tumour development and phenotype in pancreatic ductal adenocarcinoma. Gut 2019;68:487–98.
87. Singh K, Pruski M, Bland R, Younes M, Guha S, Thosani N, et al. Kras mutation rate precisely orchestrates ductal derived pancreatic intraepithelial neoplasia and pancreatic cancer. Lab Invest 2021;101:177–92.
88. Rhim AD, Oberstein PE, Thomas DH, Mirek ET, Palermo CF, Sastra SA, et al. Stromal elements act to restrain, rather than support, pancreatic ductal adenocarcinoma. Cancer Cell 2014;25:735–47.
89. Francescone R, Barbosa Vendramini-Costa D, Franco-Barraza J, Wagner J, Muir A, Lau AN, et al. Netrin G1 promotes pancreatic tumorigenesis through cancer-associated fibroblast-driven nutritional support and immunosuppression. Cancer Discov 2021;11:446–79.
90. Krishnamurty AT, Shyer JA, Thai M, Gandham V, Buechler MB, Yang YA, et al. LRRC15(+) myofibroblasts dictate the stromal setpoint to suppress tumour immunity. Nature 2022;611:148–54.
91. Krendl FJ, Messner F, Bosmuller C, Scheidl S, Cardini B, Resch T, et al. Post-transplant malignancies following pancreas transplantation: incidence and implications on long-term outcome from a single-center perspective. J Clin Med 2021;10:4810.
92. Young MD, Behjati S. SoupX removes ambient RNA contamination from droplet-based single-cell RNA sequencing data. Gigascience 2020;9:giaa151.
93. Hao Y, Hao S, Andersen-Nissen E, Mauck WM 3rd, Zheng S, Butler A, et al. Integrated analysis of multimodal single-cell data. Cell 2021;184:3573–87.

94. Jin S, Guerrero-Juarez CF, Zhang L, Chang I, Ramos R, Kuan CH, et al. Inference and analysis of cell-cell communication using CellChat. Nat Commun 2021;12:1088.
95. Yu G, Wang LG, Han Y, He QY. clusterProfiler: an R package for comparing biological themes among gene clusters. OMICS 2012;16:284–7.
96. Aibar S, Gonzalez-Blas CB, Moerman T, Huynh-Thu VA, Imrichova H, Hulselmans G, et al. SCENIC: single-cell regulatory network inference and clustering. Nat Methods 2017;14:1083–6.
97. Liberzon A, Subramanian A, Pinchback R, Thorvaldsdottir H, Tamayo P, Mesirov JP. Molecular Signatures Database (MSigDB) 3.0. Bioinformatics 2011;27:1739–40.
98. Ritchie ME, Phipson B, Wu D, Hu Y, Law CW, Shi W, et al. limma powers differential expression analyses for RNA-sequencing and microarray studies. Nucleic Acids Res 2015;43:e47.
99. Hanzelmann S, Castelo R, Guinney J. GSVA: gene set variation analysis for microarray and RNA-seq data. BMC Bioinf 2013;14:7.